SEMIEMPIRICAL MODELS OF THE SOLAR ATMOSPHERE. III. SET OF NON-LTE MODELS FOR FAR-ULTRAVIOLET/EXTREME-ULTRAVIOLET IRRADIANCE COMPUTATION

J. M. Fontenla[1], W. Curdt[2], M. Haberreiter[1], J. Harder[1], and H. Tian[2,3]
[1] Laboratory for Atmospheric and Space Physics (LASP), University of Colorado, Boulder, CO 80303, USA; fontenla@colorado.edu
[2] Max-Planck-Institut for Solar System Research, Katelenburg-Lindau, Germany

ABSTRACT

Semiempirical atmospheric models of solar surface features as observed at moderate resolution are useful tools for understanding the observed solar spectral irradiance variations. Paper I described a set of models constructed to reproduce the observed radiance spectrum for solar surface features at ∼2 arcsec resolution that constitute an average over small-scale features such as granulation. Paper II showed that a revision of previous models of low-chromospheric inter-network regions explains the observed infrared CO lines in addition to the UV and radio continuum from submillimeter to centimetric wavelengths. The present paper (1) shows that the Ca II H and K line wing observations are also explained by the new quiet-Sun-composite model, (2) introduces new low-chromospheric models of magnetic features that follow the ideas in Paper II, (3) introduces new upper chromospheric structures for all quiet-Sun and active-region models, and (4) shows how the new set of models explains EUV/FUV observations of spectral radiance and irradiance. This paper also discusses the chromospheric radiative-loss estimates in each of the magnetic features. The new set of models provides a basis for the spectral irradiance synthesis at EUV/FUV wavelengths based on the features observed on the solar surface.

Key words: solar–terrestrial relations – Sun: activity – Sun: atmosphere – Sun: chromosphere – Sun: faculae, plages – Sun: UV radiation

Online-only material: supplementary data file

1. INTRODUCTION

This paper builds upon previous work and focuses on the construction of physical models for the solar surface features observed at ∼2 arcsec resolution. The models are one-dimensional and are each characterized by temperature and height parameters given as functions of pressure. The heights are referred to an arbitrary solar radius value that is different for each model. Horizontal force balance might be invoked to obtain the height offsets between the various models, but in this paper we do not attempt to determine these offsets. The physical parameters discussed represent weighted average properties over horizontal inhomogeneities that are observed at high spatial resolution.

Frequently cited semiempirical models of the average quiet-Sun photosphere are those of Holweger & Müller (1974) and Maltby et al. (1986). However, we are not constructing a physical model for the average quiet-Sun because there are enough observations at ∼2 arcsec resolution to enable separating and understanding the radiance spectra of the network/inter-network structure in the quiet-Sun. In this paper, we provide definitions of the quiet-Sun components, and the independent one-dimensional models constructed for each of the features. These models for the inter-network and network components are used to compute their corresponding radiance spectra, which is then combined to form the so-called quiet-Sun spectrum. As discussed in Section 8, the independence of the features is only an approximation. In the present paper, we also discuss models constructed to describe plage and faculae features present in active regions, but we defer the modeling of sunspots for subsequent papers.

Fontenla et al. (2006, hereafter Paper I) developed improvements to the photospheric layers of the Fontenla et al. (1999)

set of models of quiet-Sun and active-region features based on observations at ∼2 arcsec resolution. Paper I also showed how the absolute irradiance at 1 AU computed from this improved set of photospheric models compares with recent space-borne measurements by SOLSPEC (Thuillier et al. 2003) and SORCE/SIM (Harder et al. 2005; Rottman et al. 2005) as well as Total Solar Irradiance (TSI) measurements by SORCE/TIM (Kopp et al. 2005).

Chromospheric and transition-region semiempirical models of the magnetic network features were obtained by Vernazza et al. (1981, hereafter VAL) based on EUV Skylab data and full non-local thermodynamic equilibrium (NLTE) calculations. Radiance observations at ultraviolet wavelengths (FUV and EUV) display much larger contrasts between different solar features than at most visible and infrared wavelengths and therefore allow a better discrimination and characterization of the inter-network and network features. The VAL study concentrated only on quiet-Sun areas and devised a scheme to define features on the solar surface based on a histogram of intensities at certain EUV wavelengths. Because of their different radiances these features correspond to different levels of non-radiative heating of the solar upper layers. The papers by Fontenla et al. (1990, 1991, 1993, 2002; hereafter FAL 1–4) included detailed calculation of the effects of hydrogen and helium diffusion in the ionization and energy balance of the chromosphere-corona transition region that were not considered before. These authors also studied active regions that display large magnetic fields. A set of models for most solar features at moderate resolution, including both the quiet- and active-Sun, was developed by Fontenla et al. (1999) based on the VAL observations and chromospheres, and on FAL transition-region modeling. The paper by Avrett & Loeser (2008, hereafter AL) developed an updated average quiet-Sun model (designated C7) based on matching the *SOHO*/SUMER average quiet-Sun atlas

---

[3] Currently at School of Earth and Space Sciences, Peking University, China.

of Curdt et al. (2001). As mentioned above, this model cannot be directly compared with any of the models given here because our models of quiet-Sun features correspond not to an average, but to the individual components that form the quiet-Sun.

Fontenla et al. (2007a, hereafter Paper II) presented a revision of the low chromosphere in the inter-network quiet-Sun model. This revision demonstrated that a one-dimensional, one-component model constructed for the inter-network can simultaneously account for the observations of the CO infrared lines, the observed FUV/EUV radiance spectrum, and the radio sub-millimetric and millimetric continua. The most important characteristic of this model is that it derives a low temperature minimum value that is compatible with the Ayres & Rabin (1996) model. Such a change in the low chromosphere is consistent with: (1) radiative equilibrium through most of the low-chromosphere layers, and (2) a sudden triggering of chromospheric heating as the pressure decreases below ~60 dyne cm^{-2}. In this model the heights for a given pressure are affected by parametrically-described non-gravitational forces of inertial and magnetic origin that extend the chromosphere beyond what would result from thermal hydrostatic equilibrium. The VAL and FAL papers used a turbulent pressure parameter to extend the chromosphere, whereas the new model uses a non-gravitational acceleration parameter. We remind the reader that, although the inter-network was considered non-magnetic in the past, the observations mentioned in Paper II show that important magnetic fields at the granulation scale occur in the inter-network. As discussed in that paper, these fields may have important effects on the density stratification, heating, and overall structure of the upper chromosphere.

Fontenla et al. (2008) showed that the structure of the model in Paper II is consistent with the sudden triggering of chromospheric heating produced by the Farley–Buneman instability (Farley 1963; Buneman 1963). The 2008 paper indicates that the pressure at which heating starts coincides with the point where important non-thermal line broadening starts. This supports theories that consider plasma instability to be responsible for the heating and turbulence in the upper chromosphere that is observed in the lines formed in this region (e.g., the Ca II H and K line cores).

Griffiths et al. (1998) found that several transition-region spectral features display a log-normal distribution of intensities. Warren & Mariska (1998) showed that Lyβ and higher Lyman lines have a log-normal distribution of intensities in the quiet-Sun. Fontenla et al. (2007b) also showed that the FUV continuum and Lyα display a log-normal intensity distribution but each of these with a different width. This paper also indicates that, at least in the FUV, the pixels with enhanced brightness generally correspond to increased longitudinal magnetic field observed by SOHO/MDI. The observed distribution of the FUV continuum intensities is used here to define three "levels" of chromospheric heating within the quiet-Sun, and two intensity levels within active regions. Orozco Suárez et al. (2007) used Hinode data to show that significant but small-scale predominantly horizontal magnetic fields are present in inter-network regions. These granulation-scale magnetic fields can produce magnetic heating of the inter-network chromosphere, but to a smaller extent than in network lanes where magnetic fields are stronger.

The present paper focuses on the upper chromosphere. However, because there is interaction with other layers, and because emissions in the spectrum often contain both chromospheric and transition-region contributions, we include and briefly dis-

cuss preliminary versions of the transition region (i.e., the chromosphere-corona interface) for each feature. For the analogous reasons we include photospheric layers in all the present models but limit our discussion of these layers.

In summary, we are presenting revised models of the solar magnetic features that are intended to be used for the analysis of the FUV/EUV solar spectral irradiance (SSI). This irradiance results from the contributions of the medium-resolution features of various intensity levels that are observed on the solar disk. The models in this paper differ from earlier ones as follows.

1. Relatively small changes were made to the photospheres of the magnetic models in Paper I in order to match several observations. These changes are small but relevant to the modeling of visible and IR solar irradiance.

2. Very significant changes were made to the chromospheres of the previous models to make them consistent with a sudden turn-on of chromospheric heating as indicated in Paper II in the case of the inter-network. These changes are mainly constrained by an analysis of SOHO/SUMER observations and guided by the chromospheric heating considerations discussed by Fontenla et al. (2008).

3. Significant changes were made to the transition regions of the previous models to account for the effect of revised abundances on the energy balance and emitted intensities. These changes are also constrained by an analysis of SOHO/SUMER observations. However, the modeling of these layers is not final and will be revised in future papers.

By using this set of models we compute the spectral radiance for the quiet- and active-region features for 10 positions on the disk. We then combine these radiances, as was outlined in Fontenla et al. (1999), to produce a synthetic spectrum of the spectral irradiance at 1 AU.

Some of these features are related to the so-called quiet-Sun that consists of inter-network and two levels of network. The magnetic network produces increased emission peaks in the Ca II lines and in other visible and near UV wavelengths. These peaks are less important in the inter-network regions. The recent observations by Hinode show that magnetic fields are also significant in the inter-network and therefore the separation in network and inter-network features is often only qualitative and based on spatial structure. In the UV, the network features are observed at many wavelengths, e.g., the FUV continuum, Lyα, Mg II h and k line cores, Ly continuum, and most transition lines. A number of papers dealt with the decomposition of the full-disk images into features by using different types of data, e.g., Harvey & White (1999), Preminger et al. (2001), Ermolli et al. (2007). However, because the present work is only focused on the contributions from the features to the solar spectral irradiance, the detailed spatial structure of the features is not relevant. Instead, the overall distribution of the features emitted intensity and the feature position on the disk are of interest. For this reason, we consider that the most significant precedent for our image decomposition is the VAL analysis in which intensity bins were considered. We do not, however, use the same bins structure as VAL but instead define our bins as is explained in Section 2. Also, we extend our bins definition to cover active regions with two intensity bins, and we consider sunspot umbra and penumbra features that are derived from images obtained in the visible continuum. Ideally, for irradiance studies we would like to use fixed absolute intensity bins for our
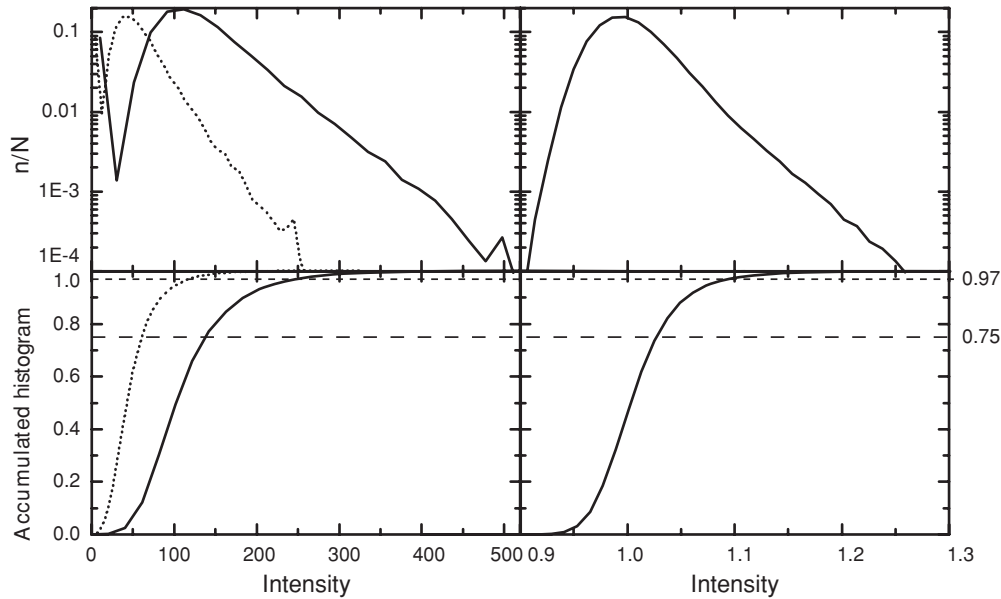
Figure 1. Histograms (top panels) and cumulative histograms (bottom panels) of the intensity for defining the quiet-Sun features. Left: continuum around the C I 1468.41 Å line (dotted line), and the core of this line (solid line). Right: Ca II K from the MLSO PSPT instrument.

decomposition, but currently we have to use relative intensities because the Ca II K line images available do not have reliable absolute intensity calibration and only have relative intensities. The method we use for the decomposition leading to the spectral irradiance calculation is described in Fontenla & Harder (2005), and the models presented in this paper are crafted for use in the computation of solar spectral irradiance as discussed in Section 3.

In the following section, we discuss the changes and the observational and theoretical basis of the models and we compare the computed spectra with current radiance observations. Also, some comparisons with available irradiance data are shown but more complete comparisons are postponed for other papers. We point out that although coarse agreement is found between the spectra derived from the present simple one-dimensional models and observations, some details cannot be matched. The reason is that the mid-resolution models do not describe the complex, time-dependent, fine structure of the upper chromosphere that is present in high-spatial resolution sequences of images taken in narrow spectral bands.

2. SUMER OBSERVATIONS

Observations by the *SOHO*/SUMER instrument have been used to produce the atlas of Curdt et al. (2001) showing the spectrum of the average quiet-Sun in the wavelength range 700–1500 Å. This spectrum is at the disk center, but spatially averaged with no discrimination between inter-network and network "lanes" or bright network patches. As part of our studies we carried out experiments in which spectra of a patch of the quiet-Sun near disk center were acquired at a spatial resolution of ∼2 arcsec. The purpose of these observations is to obtain a snapshot of the spatial variations of the radiance spectrum that are found within the quiet-Sun. We use these observations for defining a set of atmospheric models based on the distribution of observed intensities at a few wavelengths. The spatial variability of the observed spectrum can be approximately described (in a discretized form) by the results from these models. Also, the average quiet-Sun spectrum results from combining the spectrum for each component weighted by the relative area occupied by the component.

The quiet-Sun components are defined from the Ca II K line intensity enhancements as described by Fontenla & Harder (2005). Observations of the solar disk in the Ca II K line from several facilities are available. We currently use images obtained by the Precision Solar Photometric Telescope instrument at the Mauna Loa Solar Observatory (hereafter MLSO/PSPT). These data (see http://lasp.colorado.edu/pspt_access/) provide an almost continuous and accurate record since 2005 January and permit comparison of the computed with observed spectral irradiance.

Figure 1 shows the intensity distribution observed by the *SOHO*/SUMER instrument for the C I 1468.41 Å line and for a nearby continuum wavelength at 1468.82 Å compared with the MLSO/PSPT data. These data were obtained from a region of the Sun devoid of active region features, near disk center, and during the current solar cycle minimum. The figure shows that, depending on the emitted intensity formation characteristics, the histograms are similar but not identical. The figure also shows the cumulative distributions, resulting from the histograms. The median intensity in the histogram corresponds to the value 0.5 in the vertical scale of the cumulative histogram. The cumulative histogram is used to define certain ranges of intensity at each wavelength that comprise fixed segments of the vertical axis as explained next.

The histogram partitioning in categories is based on the Ca II images for historical reasons and because of the data availability. We use the letter B to designate the regions with intensities typical of inter-network, and assign to this category all pixels with intensities that correspond to values below 0.75 in the vertical scale of the cumulative histogram. The quiet-network feature is designated with the letter D and includes intensities in the range where the values of the vertical scale of the cumulative histogram are between the value 0.75 and 0.97. The active-network (sometimes called enhanced-network) feature designated as F corresponds to ranges of intensity for which the vertical scale of the cumulative histogram is above 0.97 and up to the intensity that includes all quiet-Sun pixels. The maximum observed intensity corresponds to the value 1 in the cumulative histogram vertical axis. However, the histograms have a very large value and noisy shape near the upper intensity end because of the

Table 1
Designation of Features

Feature designation	Model index	Feature Description	Pressure at 2×10^5 K (dyne cm^{-2})	Disk Center Contrast in Ca ɪɪ K MLSO/PSPT
B	1001	Quiet-Sun inter-network	0.235	<1.02
D	1002	Quiet-Sun network lane	0.340	1.02-1.08
F	1003	Enhanced network	0.552	1.08-1.19
H	1004	Plage (that is not facula)	1.00	1.19-1.43
P	1005	Facula (i.e., very bright plage)	1.62	1.43-1.80
S	1006	Sunspot umbra	3.86	. . .
R	1007	Sunspot penumbra	2.10	. . .

small number of pixels at those intensity levels. Also, even in quiet-Sun regions, microflares are observed in images taken in transition-region lines. During these events one or more pixels, depending on the location of the unresolved microflare, brighten up to very high intensity with a characteristic time of a fraction of a minute and then fade slowly with a characteristic time of a few minutes. The observations in Figure 1 contain a few of these microflares, and in the continuum data the brightest pixel reaches 7.7 times the median intensity brightness. Because of the poor statistics at the very high intensity values the histogram plot in Figure 1 does not display this range. The C ɪ 1468.1 Å line also displays brightening at the microflares locations but with a smaller contrast. The larger microflare events have been associated with X-ray brightening (e.g., Porter et al. 1995; Aschwanden et al. 2000) and often are associated with relatively faint high-speed jets. The smaller of these events correspond to the "blinkers" reported in more recent papers (e.g., Subramanian et al. 2008). Microflares are very energetic events that are not very frequent (there are only 4 out of ~40,000 total pixels that have continuum intensity more than 6 times the median value) and are not studied in the present paper.

Active regions also display a continuous intensity distribution but are different from the quiet-Sun, although plage and faculae are usually intermingled with more quiet locations and are not easily isolated spatially. The active-region Lyα intensity distribution (obtained from the SMM/UVSP instrument using observations described by Fontenla et al. 1988) has an almost flat and extended tail. This tail is superimposed onto the quiet-Sun log-normal distribution of the quiet areas present in the field of view. Similar behavior is observed in the Ca ɪɪ K line. The indication of these lines is that stronger chromospheric heating yields shallower high intensity tails of the distributions. We have not yet located detailed *SOHO*/ SUMER observations that can be used to fully characterize the active-region intensity distribution in the FUV. However, here we choose two intensity ranges in Ca ɪɪ K MLSO/PSPT data (listed in Table 1). When simultaneous and co-spatial active-region observations are located or become available we will be able to translate the intensity levels defined from the Ca ɪɪ K images to the corresponding FUV continuum levels.

Implicit in our definitions in Table 1 is the assumption that the larger intensities in the FUV continuum, the C ɪ line, and the Ca ɪɪ K line correspond to the same locations, i.e., that the relationship between intensities at all wavelengths is monotonic since all emissions correspond to enhanced chromospheric heating. This is verified between the simultaneous FUV data shown here, but is assumed in the case of the MLSO/PSPT Ca ɪɪ K data because no simultaneous and co-spatial data were available. However, the relationship between intensities at different wavelengths is not a linear one, e.g., the C ɪ and FUV continuum in Figure 1, but is often described by a power-law relationship

(i.e., a straight line in a log–log plot). Under the assumption of a monotonic relationship, intensity bins can be defined at any wavelength so as to match the same relative areas as in the Ca ɪɪ K data. With these definitions and assumptions the feature identification can be based on imaging observations at any wavelength and even in the relatively broadband (2.3 Å equivalent width) of the Ca ɪɪ K observations by the MLSO/PSPT instrument.

Yet another assumption is made in the previous discussion where we have neglected any variations of the median intensity over the solar cycle. Some indications of solar-cycle variations of the "quiet-Sun" were found by Schühle et al. (2000). Preliminary analysis also shows variations in the shapes of intensity histograms obtained from Ca ɪɪ K images. Long-term instrument radiometric stability is needed to assess such possible variations.

3. THE MODELS

The present set of models introduces new complete chromospheric layers of all components and also significant changes to the photospheric layers of the models for features other than the inter-network model in Paper II (but the photospheric layers of the inter-network model remain unchanged). These modifications revise the temperature structure and gradient in the photosphere for all cases of increased magnetic fields in order to match observations that indicate a decreased temperature gradient in the photosphere of plage and faculae, and to a lesser extent in network. We postpone for a later paper the detailed description of the photospheric layers and the comparison of the emitted visible and infrared spectrum with the observations.

In general, it is not possible to identify a particular observation or wavelength associated with only one level in the atmosphere in our chromospheric models. This is because of the extension and overlapping of the intensity contribution functions (see definition in Equation (1) of Paper II), and because our models are NLTE resulting in opacities and source functions of chromospheric lines and continua that are non-locally determined. Therefore, for the present modeling we need to consider simultaneously the entire atmospheric model, and the entire spectrum, of each feature and proceed to modify the atmospheric structure to obtain the best match of all the computed and observed spectral data. The present models aim to reproduce the observed EUV, visible, and infrared data, with less emphasis on the near UV. The reason for giving less emphasis to the near-UV is threefold: (1) observations are less complete for this range; (2) accurate atomic data for NLTE calculations is less available; and (3) the spectrum is too complex since it contains many blended lines and unknown continua (see Section 6). Furthermore, the near-UV spectrum forms in the low chromosphere where other easier temperature diagnostic, e.g., molecular lines, is available. Our method uses forward modeling and rests on trial, error, and correction based on the existing observations.

Data sets considered for development of the models presented here include quiet- and active-Sun data from *SOHO*/SUMER spectrum (also including averaged data over quiet-Sun), SMM/UVSP observations especially in Lyα, published EUV line intensity values and line ratios observed by several instruments, visible high-resolution line spectrum from Kitt Peak, and published analysis regarding the IR CO lines. Spectral irradiance observations are also used because, despite their spatially unresolved nature, they provide the most reliable absolute calibration available. Thereby, these observations provide essential clues and checks for the models because we can use the models and image analysis to evaluate the contributions to the SSI from the various features. Moreover, the models presented here are developed for use in spectral irradiance calculations and therefore their suitability for reproducing the irradiance observations is very important.

Next we briefly describe the present models, and how the observations were used to define them. In Section 4, we show how we evaluated the NLTE level populations in the models, and in Section 5 we describe how the spectrum is computed from the models and NLTE level populations and how key spectral features compared with available observations. The detailed comparison of the current model computations and the average quiet-Sun observations for these wavelengths are reviewed in Section 5.

Table 1 lists the features that were defined in Section 2 and identified by letters, and the table identifies, by a numeric index, the physical models we constructed for them. Note that, although the models correspond to the features in this table, the numbers identify the current physical models for the features designated by letters but these features are independently defined by the image analysis. Models may change in the future as new improvements are developed. Also, new features may be isolated in the solar images (e.g., coronal holes that can be found in EUV images) and new models will be created for them. Table 1 also lists the corresponding transition-region pressures at the top boundary of the models, and the ranges of contrast at disk center with respect to the median for the features defined from Ca II K observations from MLSO/PSPT images. Models S and P are listed in Table 1, but unlike the others they are identified from the PSPT images in the red band or other photospheric continuum data. The chromospheres of these models are still under development and will be further improved and discussed in a subsequent paper.

Figure 2 shows the temperature and height of the layers as functions of pressure for the models in Table 1. The distribution of height as a function of pressure is dependent on the assumed non-gravitational acceleration parameter as was thoroughly discussed in Section 3.4 of Paper II. All the values used in this paper are listed in the electronic tables available in the online edition of the journal as a supplementary tar file, and also available in the distribution files posted in the Web site http://www.digidyna.com.

Paper II described a model, numbered 305, of the low chromosphere in the inter-network feature (B), and gave preliminary values for the upper chromosphere. The present model 1001 revises model 305 by adopting a somewhat different upper chromospheric layer. Also, all our current models for magnetic features have a low-temperature minimum as was discussed in Paper II for the above mentioned inter-network model. This low value substantially differs from the FAL 1-4 and VAL chromospheric models.

The low chromospheric layers of the current models extend to pressures consistent with the onset of the Farley–Buneman
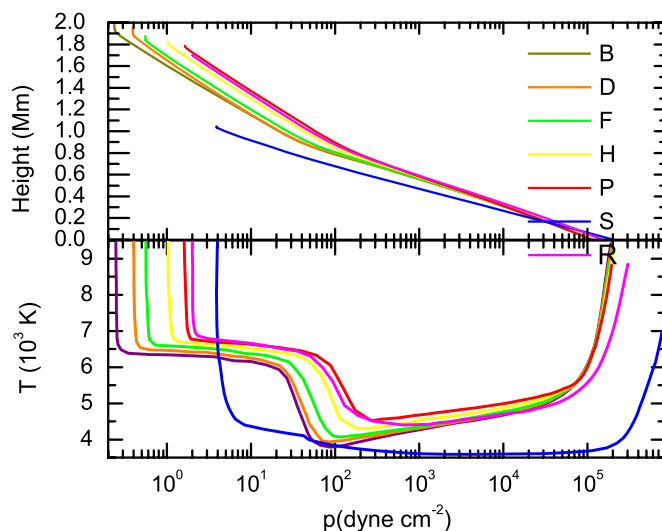
Figure 2. Temperature and height of the layers as functions of pressure for the models in Table 1. The increased slope of the height vs. pressure, at pressures below that of the temperature minimum, corresponds to a larger height-scale due to increased temperature and non-thermal acceleration in the upper chromospheres.

instability indicated by Fontenla et al. (2008) for magnetic field values consistent with network and active regions. These layers are modified from those in Paper I. Useful diagnostics for the low-chromospheric layers with temperature above ∼4500 K are provided by the CN 3883 A and CH 4300 Å bands. The line depths in these bands are significantly different for the various features, and the current models seek agreement with CN violet band head observations of the network (Liu & Sheeley 1971). The Mg I 4573 A line provides data, however we have not found observations of this line in the various magnetic features, and only quiet-Sun profiles are published (White et al. 1972). The minimum temperature value in each model was chosen to match the published values of brightness temperature increase at the bottom of the CO strongest lines. Ayres & Rabin (1996) give values for the quiet-Sun range and Solanki et al. (1996) give values for plage. These authors' definitions of network and plage are not identical to our categories but here we assume these values correspond to our brightest network and facula features, F and P, respectively. It would be extremely useful if histograms of intensity distributions were obtained at these line centers and the neighboring continua; however, this will require specially dedicated observations that are not yet available.

The temperature increase from the minimum to the chromospheric plateau is sharper than in previous models, and the upper chromospheric temperature is nearly constant in the new models. Furthermore, unlike the FAL 1-4 models, the temperature increase from the minimum to the chromospheric plateau in the new models occurs at different altitude and pressure depending on magnetic activity. The pressure at which the temperature starts to increase with height is selected consistently with the onset of the Farley–Buneamn instability as described in Fontenla et al. (2008). The most sensitive diagnostic we found for the slope of the temperature versus height increase is given by the FUV continuum. To determine this slope we mainly used SUMER spatially resolved data at wavelengths between 1400 and 1500 Å, however, as we explain in Section 6 the FUV continuum diagnostic is not simple because of NLTE effects and uncertainties in opacities.

The upper chromosphere for all models was assumed to consist of an almost constant temperature plateau as was

proposed by Avrett & Loeser ([2008](#)). However, the temperature value for the network and plage features was adjusted to match the SUMER spatially resolved FUV continuum and lines formed near the bottom of the upper chromosphere. The quiet-Sun inter-network and network intensity distribution was shown in Figure [1](#) and the models were adjusted to produce intensity levels representative of the bins mentioned there. For facula and plage we used observations of an important active region made by the *SOHO*/SUMER instrument in 2006 November.

The upper chromosphere temperature also affects the Ca II and Mg II line core emissions. However, diagnostics using these lines is complicated by the lack of absolute calibration of the observations and by uncertainties in the broadening, Zeeman effect, partial redistribution (PRD) effects, and velocities. In any case, we verify that the Ca II K line intensities observed by the $\sim$2.7 Å bandpass filter of the MLSO/PSPT instrument have intensities in plage and facula relative to the intensity for the inter-network model that are roughly consistent with those our computation produces. Also the Balmer Hα, β, and γ line centers are sensitive to the upper chromospheric temperature. Dedicated statistical studies of these lines would be very useful. Such studies can be based on the predictions of our current models and may provide important data for further refinement of the upper chromospheric models.

Another issue is the non-gravitational acceleration parameter, *accel*, as applied in the current models. As was explained in Paper II this parameter is not absolutely critical for explaining particular spectral features because a change in it can be compensated by minor changes in other parameters such as temperature values. In the present paper, we have chosen for this parameter in the photosphere and most of the low-chromosphere layers values consistent with the assumption of turbulent pressure velocity (see Paper I) and with lines non-thermal widths. Just below the temperature minimum layers we assumed a linear increase of the non-gravitational acceleration, *accel*, with height up to a value selected for the bottom of the chromospheric plateau. In this plateau, the parameter *accel* is assumed to remain constant and with the value $accel = C * g$, where g is the gravitational acceleration, and C is a coefficient of 0.219 for model 1001 and 0.255 for all other models. (Alternatively, we have tried a decreasing value of *accel* in the upper chromosphere and only find minor differences in the emitted spectrum.) These estimates are based on reproducing the available spectrum and on crude theoretical considerations about the magnetic nature of the non-gravitational force. The effects of the non-gravitational acceleration start at the layers where the plasma β is becoming not far from unity, but is still smaller than that. Assuming that the magnetic field is nearly horizontal (admittedly a questionable assumption for some magnetic features) and its strength decreases with height, then the Lorentz force can be described in terms of the gradient of the magnetic pressure, p_m, and the *accel* parameter can be expressed in terms of the gradient of the magnetic pressure divided by the mass density. In the upper chromosphere, the value of *accel* is adopted as a constant and the following equation applies:

$$p_m = p_{m0} + Cmg, \qquad (1)$$

where p_{m0} is an asymptotic value of the magnetic pressure at near-zero mass column density, C is the value indicated above, m is the mass column density, and g is the gravitational acceleration.

This formula is only a very rough expression for the *accel* parameter. The actual behavior could be much better under-

stood by studying eclipse observations at carefully selected wavelengths. We plan to examine the distribution of intensities above the limb comparing the behavior of the continuum and selected lines, and compare them with the model predictions.

The current one-dimensional modeling neglects areal variations of the features with height. Such variations are possible but not well understood. Also, near the edges of the features the horizontal radiative transfer in the chromosphere would introduce NLTE effects that make the spectral differences fuzzier at the edges. It should be noted that only a full three-dimensional modeling and radiative transfer calculation can describe, as a function of position on the disk, the occultation of lower lying regions by higher structures. In the present modeling, we do not address these three-dimensional issues, but each component feature is treated as strictly one-dimensional and radiatively independent.

The physical models in this paper only include a transition region intended to describe the part of the solar atmosphere that consists of footpoints of coronal loops. Significant changes are introduced here to the transition region of the previous models to account for the effect of revised abundances on the energy balance and emitted intensities. The basic procedure remains that of the FAL 1-4 papers, by which the downward energy flux by conduction and ionization energy transport due to diffusion nearly balances the radiative energy losses. This procedure also includes local energy deposition, and we choose certain values that are consistent with the chromospheric heating needed to balance radiative losses at the top of the chromosphere. In the current modeling, we only consider the lower part of the transition region up to temperatures of 2×10^5 K in which we carry out full-NLTE calculations as an extension of the chromosphere. The upper, and hotter, transition region and corona are optically thin at all relevant wavelengths for most viewing angles and do not require full NLTE radiative transfer calculations (see AL).

Previous transition region models describe the differential emission measure (DEM; e.g., Monsignori Fossi & Landini [1992](#)) as a function of temperature and are found in the CHIANTI 5.2 (Dere et al. [1997](#); Landi et al. [2006](#)) collection of data. The DEM formulation is valid whenever all transitions are optically thin, the two-level atom approximation is valid, and the temperature varies monotonically along the line of sight in a smooth way. Under these conditions it is meaningful to express this variation in the following differential form,

$$\mathrm{DEM}dT = n_e n_p dh, \qquad (2)$$

where n_e and n_p are the electron and proton densities, respectively, and dT and dh are the differentials of temperature and height. Assuming that a value of the pressure is given, e.g., those given in the CHIANTI data, this equation can be integrated to produce values of temperature versus height corresponding to the tabulated DEM values.

The comparison in Figure [3](#) shows fairly good agreement between some of our models and the results from integrating the DEM given by CHIANTI 5.2, for temperatures above 6×10^4 K in the quiet-Sun. However, for lower temperatures the agreement is poor because the DEM method cannot describe the optically thick lines formed at low temperatures. At higher temperatures the temperature versus height curves are similar, but our models for quiet-Sun components have higher pressure than the CHIANTI 5.2 values. Also, these DEM data do not distinguish between the inter-network and
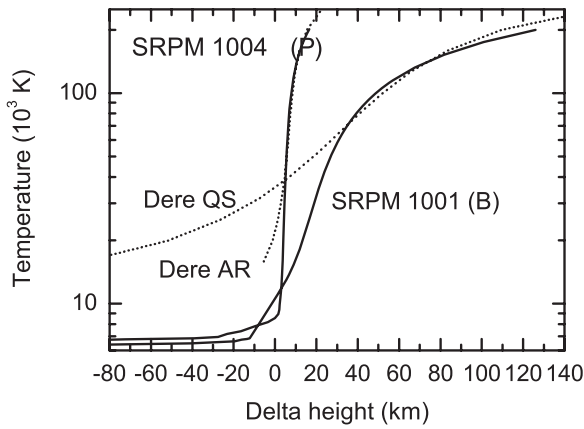
Figure 3. Transition region of some of our models compared to the structure derived from the DEM values by Dere that are given in CHIANTI 5.2 (see Dere et al. 1997) for quiet-Sun and an active region. The structures derived from the DEM assumed a pressure of 0.142 dyne cm^{-2} for the quiet-Sun and 1.6 dyne cm^{-2} for the active region. (For the structures derived from DEM the He partial pressure was disregarded.)

Table 2
Atoms or Ions and Levels Computed in full NLTE

Species	NLTE Levels	Species	NLTE Levels	Species	NLTE Levels
H I	15	. . .	. . .	. . .	. . .
He I	20	He II	15	. . .	. . .
C I	45	C II	27	C III	38
N I	26	N II	33	N III	39
O I	23	O II	31	O III	44
NA I	22	. . .	. . .	. . .	. . .
MG I	26	MG II	14	MG III	54
AL I	18	AL II	14	Al III	32
SI I	35	SI II	14	SI III	60
S I	20	S II	30	S III	32
CA I	22	CA II	24	. . .	. . .
FE I	120	FE II	120	. . .	. . .

network, and therefore this comparison is not completely consistent.

4. DEPARTURES FROM LTE

For the present study full NLTE radiative transfer calculation was carried out in all the important species listed in Table 2. We also performed NLTE computations for H. For H the calculations include particle diffusion as discussed in FAL 1 and 2. We are re-analyzing the assumptions made in FAL 3 and 4 regarding the helium abundance and consequently have not yet included the He particle diffusion. Also, we are not considering the diffusion of other species here. In the full NLTE calculations, we consider 28 low-ionization species, 981 bound levels, and 12,278 spectral lines of the species in Table 2. Radiative rates of lines with gf smaller than 10^{-6} were neglected.

Higher ionization species are not listed in Table 2, but are computed in the optically thin approximation by solving the statistical equilibrium equations for all levels and species included in the CHIANTI 5.2 data (Landi et al. 2005) and neglecting the upward radiative transition rates. Currently, ionization and recombination transitions into various levels are also neglected in these optically thin calculations and will be included when reliable atomic data become available. These choices are based on the AL results concerning which species are severely affected by optical thickness effects. Full NLTE calculation of Ne and Ar at ionization stages III and smaller have not yet been carried out because, despite having abundances in the range we considered, these species are not important for the results shown here. However, higher ionization stages of these elements were included.

For most computations in this paper we use our solar radiation physical modeling (SRPM) computing system. However, for comparisons we used the PANDORA computer program of Avrett & Loeser (2003). The PANDORA runs we compare used the same heights, temperatures, and total hydrogen density as in model 1001, but the ionization, level populations, and electron density are re-calculated.

Table 2 gives the number of levels considered explicitly in our NLTE radiative transfer calculations for each species. In this paper, we do not combine similar energy levels into "super-levels," as is done by other authors. Our rationale is that level

population ratios are affected by spontaneous transition rates of permitted lines that are generally much larger than collisional rates. Consequently, we do not assume an LTE relationship between any levels, but instead determine whether such a relationship exists or not. However, all levels considered here include sublevels corresponding to the different values of the quantum number J. The lines are treated in full detail with all the multiplet components for the upper and lower sublevel values of J; and we only assume that all sublevels of the same level are populated according to a Boltzman relationship. The validity of this approximation still needs to be demonstrated in each species.

Because most lines are treated explicitly as mentioned above, we do not use any "line haze" opacity in the SRPM NLTE calculations or computed spectrum. However, we did not consider on the photoionization processes the effects of absorption or emission lines from elements other than hydrogen. Many absorption lines are observed in the near-UV and emission lines are observed in the FUV and EUV, but we postponed considering these. Furthermore, for the main calculation "extra" continuum absorption and emissivity were added. In Section 6 we discuss the effects and rationale behind these choices and how they relate to the issue of the "missing" UV opacity. In the present calculation, we have not yet included irradiation from the upper transition region and corona (at $T > 2 \times 10^5$ K). This irradiation is significant in the upper chromosphere, but it would be absorbed by these layers and would have little effect in deeper layers. We will include this irradiation after developing the corresponding coronal and upper-transition-region models for each of the features we consider.

For many transitions, SRPM used published collisional strengths computed using detailed quantum-mechanics methods. However, in other cases collisional strengths were obtained from the Seaton (1962) approximation. The collision strengths are being continuously updated as more reliable data become available and are entered in the SRPM system. Currently collisional excitation by protons is neglected, but excitation by collisions with neutral H is included as described in Paper II.

Figure 4 shows some of the resulting coefficients of departure from LTE (or NLTE departure coefficients) defined by the ratio of the calculated level populations relative to those resulting from the Saha–Boltzman equation with the given ion and electron densities. Generally the departure coefficients for levels with energy close to the continuum are not far from unity, but in the low-chromosphere overionization causes them to be below unity at and somewhat below the temperature region. The top
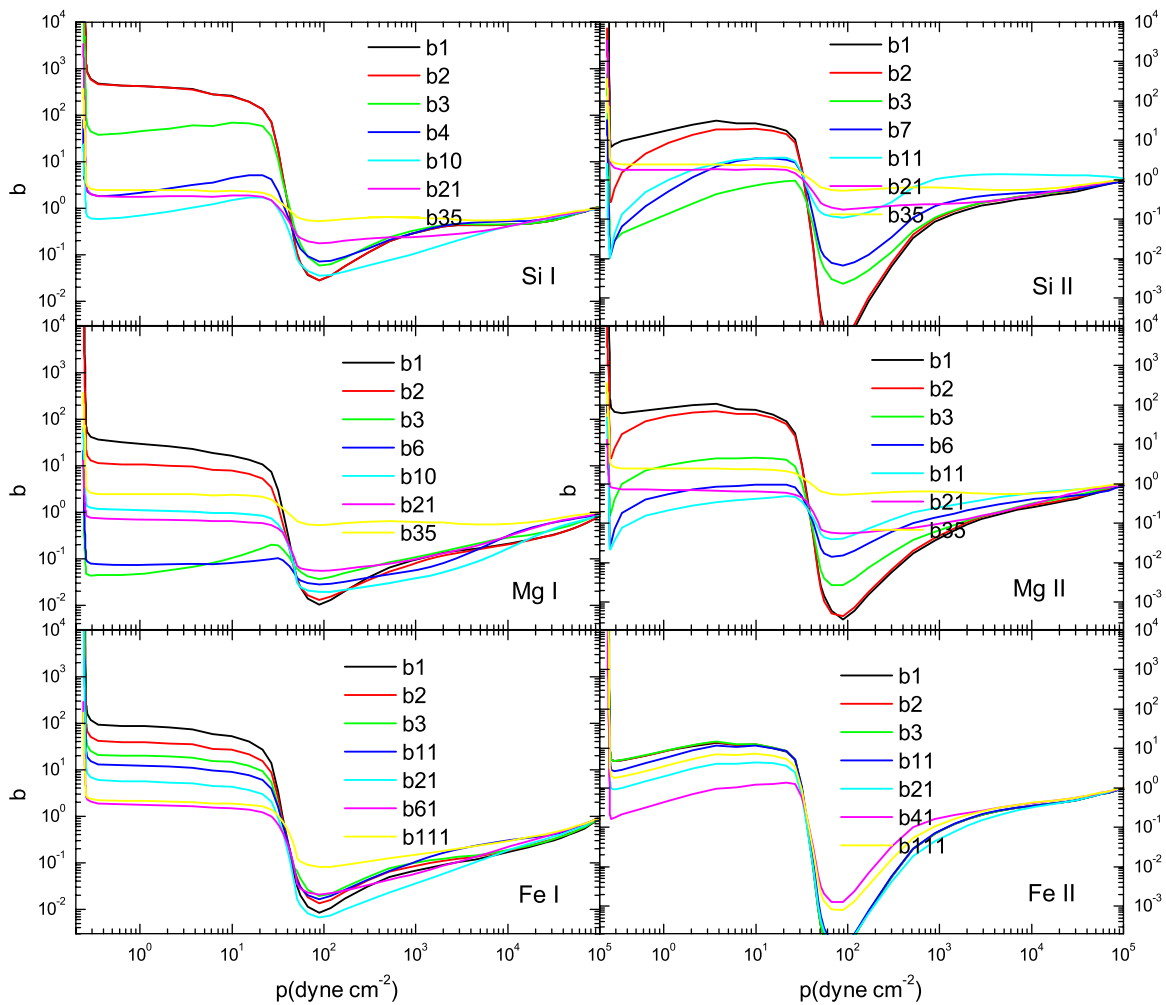
Figure 4. *b*-coefficients measuring departures from LTE in model 1001 (feature B) for selected levels of several species. The index of the levels plotted (levels are indexed according to their energies) are indicated in the legend in each panel.

levels in our calculation have ionization energy values less than 1 eV in most cases.

Because of the NLTE effects, the line source function shows a much more gradual variation with pressure (and with height) around the temperature minimum than does the Planck function. This decoupling of the source function from the Planck function prevents the use of wings of strong lines, e.g., of the Ca II lines, to meaningfully determine the temperature structure around the temperature minimum. A diagnostic of the local temperature cannot be directly based on such NLTE lines because the line source function behavior depends in a complicated fashion on the continuum and line opacity and the model global temperature structure.

All our results display overionization (i.e., ground-level departure from LTE coefficients smaller than unity) of all species around the temperature minimum. Instead, underionization (i.e., ground-level departure from LTE coefficients larger than unity) occurs in the upper chromosphere. Also, near the temperature minimum the lower levels have smaller departure coefficients than the upper levels, indicating that the overionization of neutrals is a result from FUV and/or EUV irradiation which primarily affects lower levels. This indicates that overionization is much more affected by the irradiation from the upper chromosphere in continuum and emission lines than by the photospheric radiation and absorption lines. Therefore, we stress that the con-

sideration of a realistic upper chromosphere is essential to the determination of the densities near the temperature minimum of (1) neutral low first-ionization-potential (FIP) elements, and (2) singly ionized high FIP elements. Even a very sophisticated calculation of the effects of lower chromospheric absorption lines on the elemental ionization can produce unrealistic results if it does not include upper chromosphere irradiation.

To assess the effects of the "extra" opacity and emissivity (described in Section 6) and different NLTE methods, we compared our SRPM calculated results for model 1001 (feature B) with those using PANDORA, where "super-levels" and "line-haze" opacities are included. Both calculations show the same trends and are not dramatically different. However, minor variations are found which are likely due to differences in collision rates, the grouping into super-levels, and to a lesser extent, due to the different background opacity and emissivity adopted in both cases.

Figure 5 shows some of the comparisons between SRPM and PANDORA computations of the NLTE departure coefficients. Differences between these results include: (1) the number of levels and grouping; (2) use of "extra" continuum opacity and emissivity in SRPM and the "line-haze" opacity and emissivity in PANDORA; (3) collisional rates; (4) photoionization cross-sections; and (5) the sets of wavelengths used for determining the radiative transition rates for lines and continua. Another
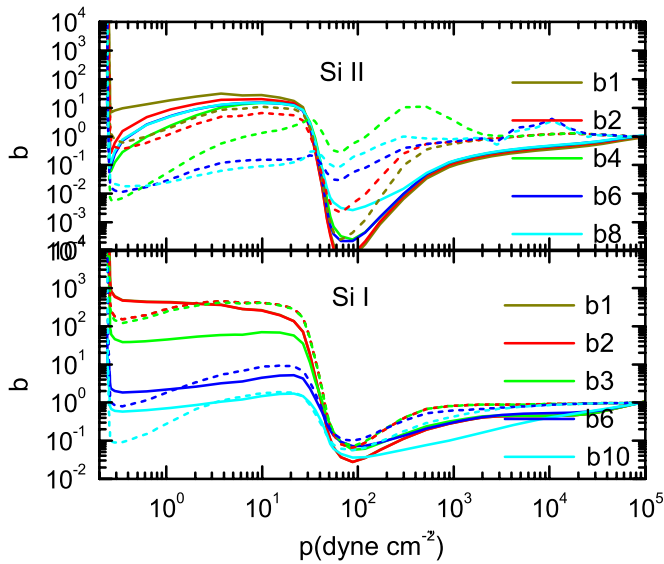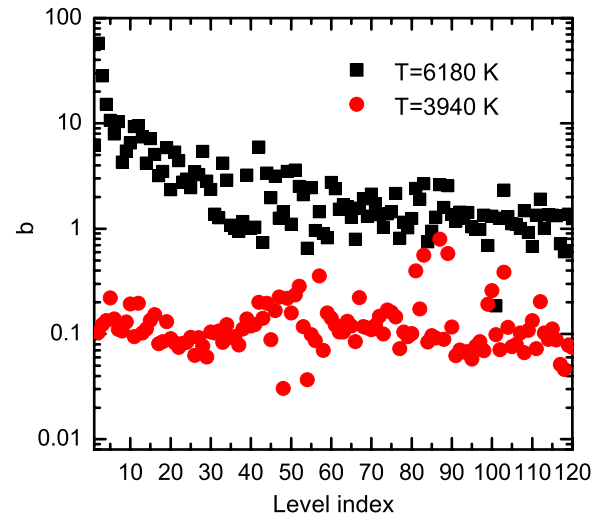
Figure 5. NLTE departure coefficients for Si I and II in model 1001 (feature B), computed using SRPM (solid line) and using PANDORA (dash line). The general behavior is similar in both cases, but differences are present especially for Si II.


Figure 6. NLTE departure coefficients for Fe I as functions of the atomic level index for various altitudes (the labels indicate the corresponding temperatures). Black, the upper chromosphere; red, near the temperature minimum.

difference between the two methods is that SRPM only computed in detail all the atomic levels specified in Table 2 and used the very detailed CHIANTI 5.2 set of levels with the optically thin approach for the higher ions, but the PANDORA calculations used a set of super-levels and did not use any optically thin approximations. Yet another difference is that the SRPM NLTE method is based on an extension of the method by Fontenla & Rovira (1985a, 1985b) that uses a pseudo-Newton-Raphson simultaneous multi-level solution, while PANDORA uses an equivalent two-level atom approach described by Avrett (2009).

Given all these differences, the agreement between the trends in both computations verifies that the basic points of this paper are sound. For the present runs the Si II computation of NLTE by SRPM used collisional strengths produced by using the Seaton formula, while PANDORA used more accurate data from Dufton & Kingston (1994). Also, SRPM followed its standard of leaving all different J as sublevels of the same level, and in PANDORA several of the sublevels in the lower levels were considered as independent levels. Furthermore, SRPM considered a number of higher lying levels that were omitted in PANDORA. For some of the Si II ion transitions effective collision strength data exist in CHIANTI; however, this source of data does not cover all transitions we studied. We are continuously updating the SRPM values to the best currently available data and meanwhile we regard our computed Si II spectral lines as rough estimates. Figure 5 also shows the NLTE departure coefficients for Si I and in this case the agreement between SRPM and PANDORA is much better. Again, SRPM used the Seaton formula for the collisional strengths and PANDORA used the values given by Cincunegui & Mauas (2001). These collisional strength values are not very reliable because they do not derive from detailed quantum-mechanics calculations. Here, again there are differences in that PANDORA combines certain levels that SRPM treats individually, but this is not the case for the lower most levels, several of which are shown in Figure 5.

Another important point is that in the chromosphere the departures from LTE of the upper levels of low-FIP elements follow a certain trend, as shown for Fe I in the Figure 6

example. At any given pressure (or height), the departure coefficients approach unity as the level energy increases, and these coefficients for the topmost levels are not far from unity in the upper chromosphere. However, as mentioned earlier, all the computed coefficients remain smaller than unity near the temperature minimum due to the irradiation from above that drives the lower level coefficients to small values. Figure 6 also shows fluctuations around the trends. These fluctuations are due to the structure of radiative transitions connecting the various levels. The overall behavior suggests that one could only solve in detail the statistical equilibrium equations for fewer levels than considered here. Then, one can consider the higher energy-level populations using the Boltzman relationship with respect to the uppermost explicitly computed level. Figure 6 shows that in the case of Fe I the asymptotic values are reached for about level 72 (of configuration 3d7(4F)5s-e 3F), with an excitation energy of ∼0.752 of the ionization energy and an ionization energy of ∼1.97 eV. (However, at energies very close to the continuum the quasi-static fluctuating electric fields produce a merging of the levels above those considered here.) Note, that even when the population statistical equilibrium equations for many high-energy levels do not need to be computed, the transitions between these levels and those computed explicitly must be included in the computation of lower levels and ionization. This can be done in a way similar to the merging of upper levels with the continuum used by Mihalas et al. (1975). Otherwise, incorrect populations would result for the topmost explicitly solved levels.

5. COMPUTED SPECTRA

Spectra with very high spectral resolution were computed with variable wavelength sampling in which all line profiles are described by at least 20 points. This was done for all of the models in Table 1 at EUV/FUV, visible and infrared wave-length ranges, and at 10 disk positions. (We choose 10 equally spaced values of $\mu=\cos(\theta)$, where θ is the angle between solar radius and viewing direction, covering from 0.1 to 1.) We show representative results that demonstrate how the computations compare with high-spectral-resolution observations that are not absolutely calibrated, as well as with low-resolution observations that have radiometric calibration. From the comparisons,
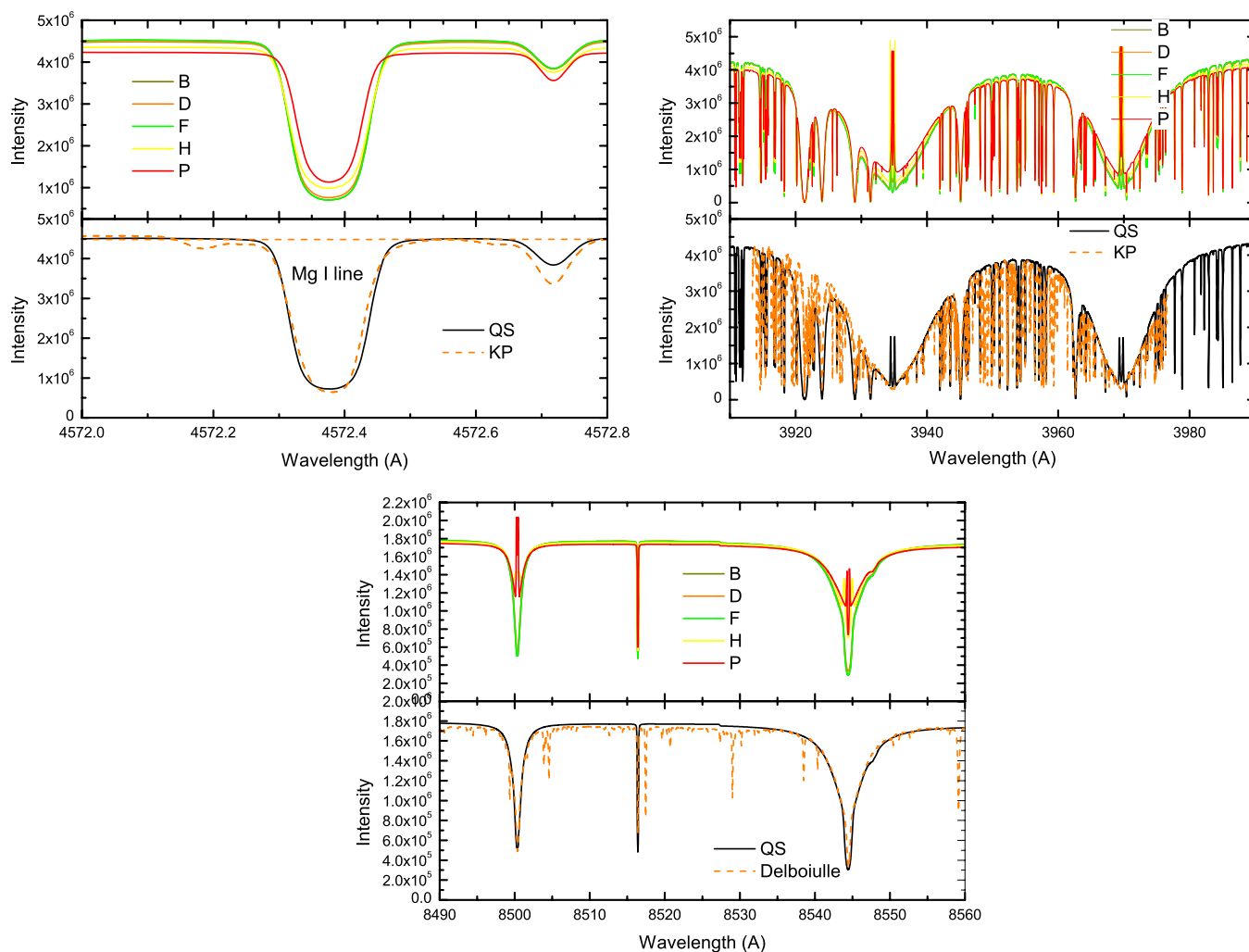
Figure 7. Several high-resolution spectral lines computed from the present models and compared with the Kitt Peak quiet-Sun atlas (Wallace et al. 1998) for the disk center. In the case of the Ca II IR triplet, the comparison is with the Delbouille et al. (1981) atlas. Panels (a) semi-forbidden Mg I 4573.77 Å (vacuum wavelength) line; panels (b) the Ca II H and K lines (we have not used PRD for these computed Ca II lines and therefore the K2 peaks are not accurate); panels (c) two of the Ca II IR triplet lines. In each panel, the upper subpanel shows the spectrum at disk center for five features modeled and the lower subpanel shows that for the average quiet-Sun mix of three features. In all cases the Kitt Peak and Delbouille data, which are referred to the continuum, were scaled to match the continuum computed for the quiet-Sun combination.

we conclude that the current models still yield values at blue wavelengths in the visible range that are a few percent higher than the observed absolute irradiance. However, the models in combination with the full-NLTE computations produce high-resolution results that compare very well with the observed atomic line profiles. Figure 7 shows the comparison with Kitt Peak data (Wallace et al. 1998) of several lines in the visible. Likewise, the calculations of molecular lines shown in Figure 8 match very well with the high-resolution observations when the continuum is well defined and computed. This figure shows the results in the G-band, and the CN band head at 3883 Å. In all cases, the Kitt Peak spectrum was "normalized" to match the computed continuum intensity, and wavelengths were converted to vacuum. This figure also shows, in the upper panels for each case, the results for each of the models, and thereby the intensities for various levels of magnetic activity.

The top panel of Figure 9 shows the emergent intensity of the various models at EUV/FUV wavelengths. The lower panel shows our standard average quiet-Sun combination (namely QS = 0.75 B+0.22 D +0.03 F) compared with the *SOHO/ SUMER* quiet-Sun atlas. At wavelengths between 912 and 1100 Å, the computed continuum is somewhat higher than the

observed, but at wavelengths between 1320 and 1450 Å the computed continuum is somewhat lower.

This figure shows a few computed absorption lines that are not observed. These computed lines are formed in the upper chromosphere of our models and correspond to transitions whose collisional strengths are not well known. There are also several unobserved (e.g., SORCE/SOLSTICE) edges in our computed spectra. The computed intensity increases at wavelengths longer than the Si II $\sim$1521 Å photoionization edge from the ground level. The Si I level 2 photoionization edge occurs at $\sim$1680 Å and has a small cross-section. It is possible that this cross-section is underestimated by the TOPBASE data we use, and it is also possible that our level-2 population is underestimated due to a too low collision strength for transitions between levels 1 and 2 in our Si I atom. The photoionization edge from the ground level of Fe I occurs at $\sim$1569 Å, but the atomic data we use (from Bautista 1997) have about 10 times smaller cross-section than the Si I photoionization from the ground level. Also, the photoionization from level 2 of Fe I occurs at $\sim$1760 Å and has a similarly low cross-section. The continuum intensity in the range $\sim$1521–1760 Å would be lower if these cross-sections were underestimated or if the Fe I ionization was overestimated
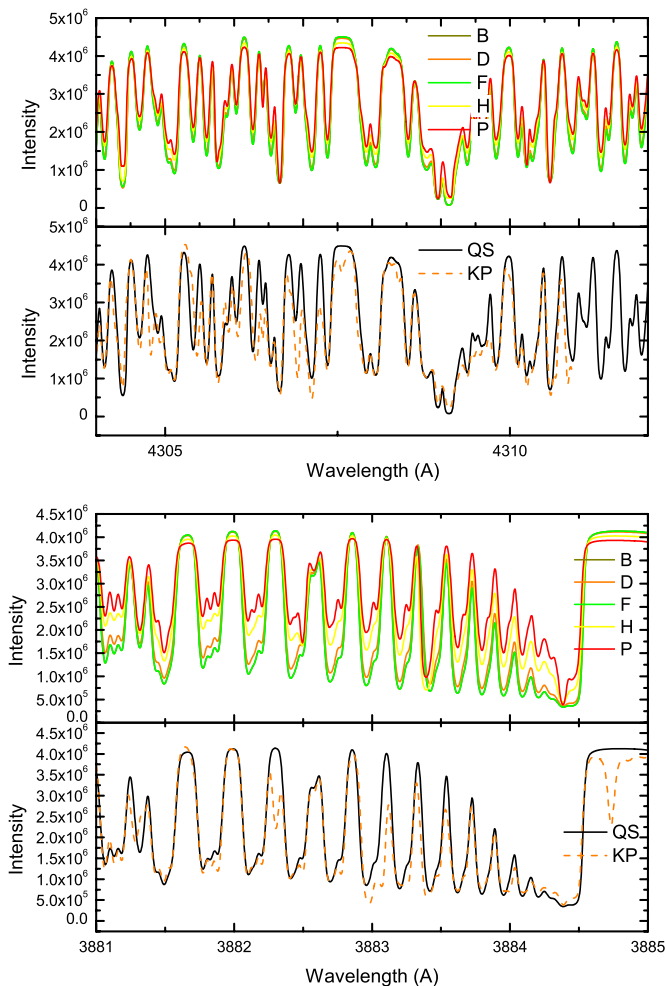
Figure 8. Molecular lines with well-determined continua. Panels (a) G-band of CH molecular lines, panel (b) the violet CN band. In each panel, the upper subpanel shows the spectrum at the disk center for five modeled features and the lower subpanel shows that for the average quiet-Sun mix of three features. In all cases, the Kitt Peak data were scaled to match the continuum computed for the quiet-Sun combination.
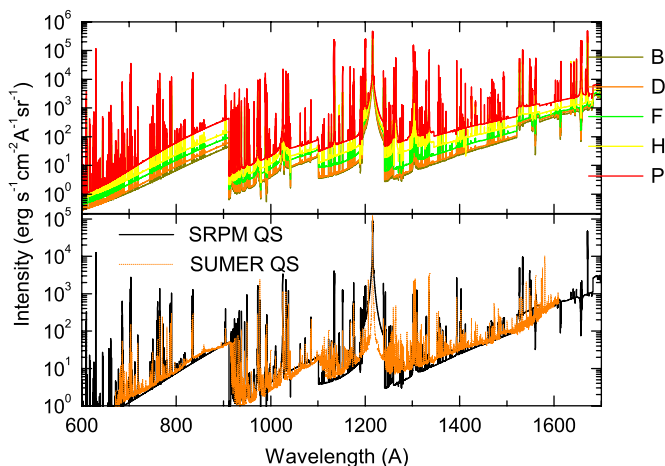
Figure 9. Emergent intensity EUV/FUV spectra computed for five feature models (top panel) and the spectrum for the average quiet-Sun mix of three features compared with the *SOHO*/SUMER atlas of the average quiet-Sun (bottom panel). Coronal and upper transition-region emissions are not included in the plotted calculations. The intensity units are erg s^{-1} cm^{-2} Å^{-1} sr^{-1} or equivalently mW m^{-2} Å^{-1} sr^{-1}.
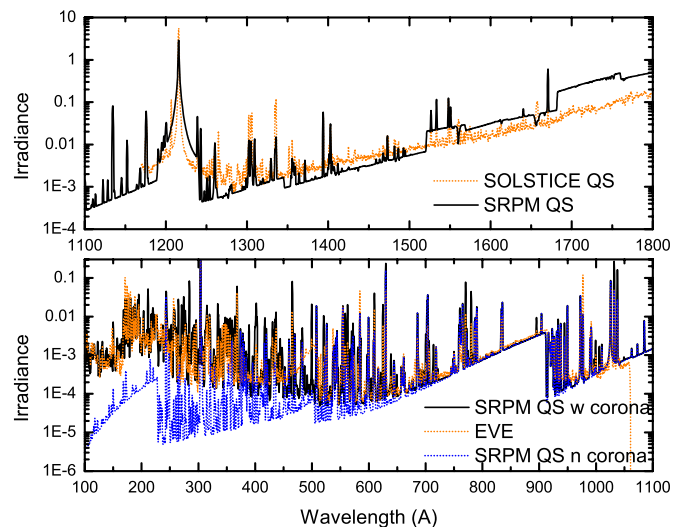

Figure 10. Comparison of the computed quiet-Sun irradiance spectrum at 1 AU (computed for the standard quiet-Sun mixture of components, see the text) with the observations by SORCE/SOLSTICE (upper panel) and by a sub-orbital flight of the EVE instrument (lower panel) on a day of very low solar activity during the past minimum. Computed coronal and upper transition-region line emissions are included in the black solid line in the bottom panel, but are not included in the blue dotted line. The coronal and upper transition-region contributions dominate at wavelengths shorter than 600 Å. The SRPM data were convolved to the instrument resolution (~1 Å) in both panels. The irradiance units are erg s^{-1} cm^{-2} Å^{-1} or equivalently mW m^{-2} Å^{-1}.

in our calculations. At ~1622 Å the photoionization edge from the ground level of Mg I occurs, but its cross-section is even smaller than the Fe I ones.

Because the observations indicate that no significant edges are observed up to wavelengths ~2000 Å, it is possible that another more important continuum edge around that wavelength renders the edges mentioned above unobservable. The edge in the observed spectrum at ~2000 Å is usually attributed to the Al I 2071 Å photoionization from the ground level, which has a large cross-section. The Si I 1986 photoionization edge from level 3, and the Fe I 1932 Å photoionization edge from level 3 are very close to the Al I edge, and in our calculations they all contribute to the computed emergent intensity variation at ~2000 Å. However, our calculations taking into account all these species display a jump much smaller than the observed. If some of these photoionization cross-sections were much larger than our data indicates, then this jump would be larger and could erase the other edges. In Section 6, we discuss the issue of "missing" FUV opacity that is related to these matters.

Figure 10 shows the solar irradiance for a quiet-Sun day (2008 April 14) computed by SRPM from the present models and the spectra observed by the SORCE/SOLSTICE instrument (Woods et al. 2009) and the EVE instrument on a rocket flight (Chamberlin et al. 2008). For these comparisons we convolved the SRPM profile with instrument profile functions with FWHM=1 Å width that try to represent the SORCE/ SOLSTICE and EVE instruments. The SRPM irradiance spectrum was again constructed by using the standard combination of quiet-Sun features. The comparisons now include the optically thin emission lines from the upper transition region and the corona that were computed using the coronal models of M. Haberreiter & J. M. Fontenla (2009, in preparation). However, the coronal and upper-transition region bound-free continua are not yet included. For wavelengths shorter than ~600 Å the coronal and upper transition-region lines dominate the spectrum.
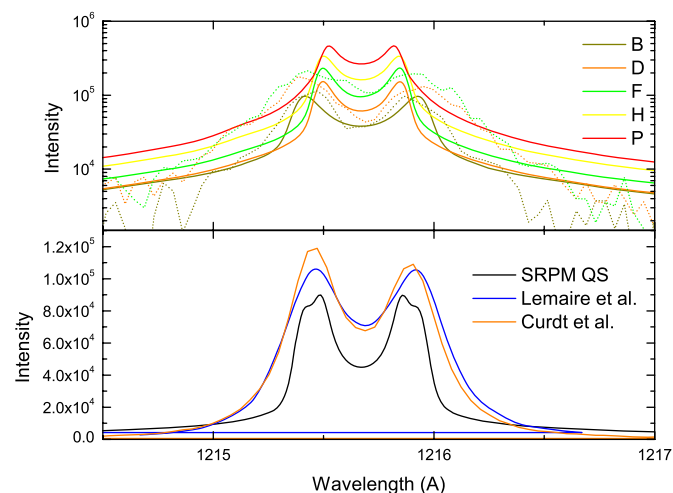
Figure 11. Computed and observed Lyα line. The top panel shows (with a logarithmic vertical scale) the computed line for our models (except for sunspots) and observation from *SOHO*/SUMER for several pixels in the quiet-Sun network (dotted lines). The lower panel shows (with a linear vertical scale) the computed quiet-Sun profile compared with the average quiet-Sun near the disk center from *SOHO*/SUMER (for 120 positions along the slit; Curdt et al. 2008), and with the full-disk spectrum by Lemaire et al. (2005).

Note that the *SOHO*/SUMER disk-center intensity spectrum shown in Figure 9 displays an increasing trend above ∼1500 Å that is not observed in the SORCE/SOLSTICE irradiance spectrum in Figure 10. It has been suggested that an explanation for this increasing trend is contamination by the second order. This effect has not been corrected in Figure 9, but Section 6 shows that this effect only explains part of the trend in the *SOHO*/SUMER data.

5.1. The Lyα Line

Figure 11 shows the computed Lyα line emergent intensity profile compared with observations by *SOHO*/SUMER on 2008 June 26 (see Curdt et al. 2008; Tian et al. 2009). This was a period of very low solar activity. The upper panel compares Lyα profiles computed for the quiet-Sun models with the *SOHO*/SUMER observations at several pixels. This figure also shows profiles from plage and facula to illustrate the range of values computed for these magnetic features. The spatially resolved quiet-Sun observations show a large variety of intensities, central reversals, and asymmetries, some of which were described by Curdt et al. (2008) and were also addressed by Fontenla et al. (1988) from SMM/UVSP data. The lower panel shows a *SOHO*/SUMER profile, that results from averaging over 120 pixels, and the average spectrum by Lemaire et al. (2005), compared with the computed SRPM average quiet-Sun composed by the weighted average of the profiles from the standard mix of quiet-Sun features. The comparison shows that the computed line peaks are somewhat small compared to the observed average, but a minor increase in the transition region pressure can increase the computed peaks.

The spectral feature displayed in the computed peaks of the average quiet-Sun spectrum is due to the mix of components B and D (component F is also present but with very low weight). The distance between the peaks is sensitive to the turbulent broadening velocity at the top of the chromosphere and in the low transition region. The computed peaks are narrow, but because the non-thermal line broadening in the chromosphere and transition region of model B is assumed to be larger than that for model D, the peaks in B are slightly more separated

than in D as the upper panel of Figure 11 shows. This choice in the models corresponds to the observed larger broadening and velocities in the inter-network. However, the structure in the line profile peaks is not observed but instead broader peaks are observed. A simple explanation for this discrepancy is provided by the spatially resolved data. The explanation is that we use only three static components to describe the continuous range of intensities, broadening, shifts, and asymmetries that are observed.

The far wings ($\delta\lambda > 1$ Å) in our current computation are too high, and this issue is related to the PRD characteristics along with the line broadening. In our computations we assumed collisional broadening using a Voigt profile and that may not be very accurate in the far wings where the Holtzmark broadening effect dominates.

A more serious issue is that of the near wing broadening. In nearly all pixels, the observed profiles show a near wing that is less steep and broader than our results. Although that could also be related to the PRD to some extent, we believe the larger broadening is due to other effects. Temporal fluctuations of line shift could be responsible for the larger broadening but the exposure time was relatively small, i.e., 15 s. Very fine spatial-scale unresolved motions could broaden the line as observed and we note that granulation scales are not resolved by the 1 arcsec pixels of *SOHO*/SUMER. Fontenla et al. (2008) proposed that the non-thermal broadening velocity may be species dependent. Also, other sources can affect the line broadening such as small-scale magnetic fields or electric fields that can broaden the line. Note that polarization observations in this line at very high spectral resolution could answer some of these questions. Regardless of the physical mechanism, the observations shown here suggest that the hydrogen line's non-thermal broadening velocity value should be increased in the top of the upper chromosphere of all models.

5.2. Line Ratios and Transition-region Pressure

A strong constraint on the transition-region pressure is given by the observational diagnostic based on density sensitive line ratios (e.g., Doscheck et al. 1998). However, the method employed in these determinations assumes the pair of lines used and all transitions between related levels are optically thin. As shown by AL, this is the case only for transition region lines formed at temperatures above ∼6 × 10⁴ K. For many lines (e.g., Si III lines that have been used in the literature) it is likely that at least one of the lines in the pair used, or one of the other related transitions, is not optically thin and thus the simple method would give an erroneous density because the line ratio would be different from the expected value at the correct density. Furthermore, in some cases one of the lines in the pair used is very weak, or blended, and the continuum subtraction is subject to uncertainty. An example is the Si III line pair used in the literature in which the weak line at 1301.146 Å overlaps the wing of a very strong O I line on one side and the 1300.9 Å line on the other side. In addition, this blending makes the optical pumping of this Si III transition possible.

The intensity ratio of the Si III 1296.725 and 1301.146 Å lines in the presently computed quiet-Sun composite has the value 1.3, which is somewhat lower than the value 1.59 observed by Doscheck et al. (1998) and would correspond to higher pressure in their method. However, these lines are affected by non-optically thin effects; therefore, electron density values derived from the ratio between these lines under an optically thin assumption are not meaningful.

For other lines such as the O v 759.441 and 761.128 Å lines, the optically thin condition is much more certain. The electron density values derived from the ratio of these O v lines near the disk center by Doscheck et al. (1998) give $p = kT(n_e + n_H) \sim 0.3$ dyne cm^{-2}. In our computation of the quiet-Sun combination the ratio between these O v lines is 5.2. This is slightly lower than the values given by Doscheck et al. (1998) in their Table 1, ranging from 5.4 to 6.9 except for the extreme single values of 9.4 and 1.59. As was shown in our Table 1 earlier the first two components of quiet-Sun have pressures close to that obtained by Doscheck et al. for the quiet-Sun. However, the peak intensities of these two O V lines are severely overestimated by our present computations because their peak formation temperature is just within our top boundary condition points. For the active region model 1004 (feature H) we find from SRPM results the ratio 2.2 between these O v lines. This ratio is slightly higher than the values 1.43 and 1.8 for active region bright kernels in Doscheck et al. (1998) and would correspond to a less active feature. Note that these authors obtain a low value of $\sim$1.0 for an explosive event which probably corresponds to an extremely high pressure, and they obtain values in the range 1.34–2.3 for bright kernels near a sunspot.

In our computations the ratio of the O IV 1399.77 Å to the Si IV 1401.16 Å line intensities (after subtracting the continuum) yields 0.23 for the quiet-Sun combination of features. Doscheck & Mariska (2001) give the value of the O IV/Si IV ratio as $\sim$0.27 for the average quiet-Sun; but their Figures 1 and 2 show the variability of this ratio and that it tends to decrease to around 0.2 for brighter Si IV pixels. Using the *SOHO*/SUMER quiet-Sun spectrum (and again subtracting the continuum), we find this ratio to be around 0.18. However, in our current calculation both of these lines have an absolute intensity a few times larger than the observed values. This can be due to a too shallow temperature gradient in the transition-region model at $T \sim 10^5$ K. Alternatively, a smaller than unity filling factor can account for the differences between the computed and observed transition-line intensities.

Warren et al. (2008) finds pressure values in very bright active region "moss" that are broadly consistent but somewhat higher than those in our model 1005 (feature P). Their values were derived from high temperature ions that are present in the upper transition region and corona. However, these authors invoke a filling factor that changes dramatically with height within the transition region on the basis of some theoretical models that predict very high pressures at the footpoints. Instead, our models have no significant variation of the pressure along the lower part of the AR loops, do not have such high density at the footpoints, and do not require such a strongly height-dependent filling factor. Although it is likely that the available observations do not resolve all the spatial structure, in our models it is not necessary to assume a large variation in the filling factor over the lower portions of the legs of active-region coronal loops. We believe that the problem with the theoretical models mentioned in Warren et al. (2008) is produced by their lack of consistency in the computations of the radiative losses and energy transport in the transition region. When consistent computations are carried (see FAL 1–4) there is no need for a strongly height-dependent filling factor value.

Using *Hinode* EIS data for lines formed in hotter regions of active region loops, Tripathi et al. (2008) find for the active region "moss" values of $n_e \sim 10^{10}$ cm^{-3} for $\log T = 5.8$–6.1. These values are consistent with our model 1005 for feature P, i.e., facular regions.

From the described line-ratio data, and because of the good agreement of the very pressure sensitive Lyα line with the observations, we find that the transition region pressures in our quiet- and active-Sun components are fairly consistent with the observations. However, our current computations give too large intensities of many transition region lines; for this reason we cannot rule out the need for a filling factor which would be independent of height, at least within the lower transition region.

5.3. Detailed Line Profiles

The lines of the most abundant species in the upper chromosphere are extremely temperature sensitive, but there are sometimes significant effects due to charge transfer with hydrogen and helium. Other known effects are due to optical pumping by overlap with strong lines that can skew the level populations from the otherwise expected (a well-known example is the optical pumping of O I by Lyβ).

The present transition-region part of the models is preliminary because we have not yet determined the temperature as a function of height in a way that is fully consistent with energy balance. To establish the transition region in our models we used the basic procedures described in FAL 1–4. In these papers, the expressions used for the radiative losses functions were based on the data from Cox & Tucker (1969). Instead, in the present calculations we have modified these to use the current abundances and atomic data. However, the NLTE calculations we carry out in the present paper give significantly different radiative losses that are described in Section 7. Consequently, our transition-region models will have to be further modified for using the currently computed radiative losses through an iterative procedure.

In general, for the current models, the computed transition-region lines formed at temperatures larger than $\sim 5 \times 10^4$ K are stronger than the observed (e.g., the C IV 1548.2 and 1550.8 Å lines and the Si IV 1393.8 and 1402.8 Å lines). The lines formed at temperatures lower than $\sim 2 \times 10^4$ K are usually weaker than the observed. The Si III lines connecting our level 2 (metastable) to 5, namely 1294.545, 1296.726, 1298.9 (with two components), 1301.149, and 1303.323 Å, shows narrower profiles than the observed and their computed peak intensity is about 10%–30% lower than the observed. The line-center intensities of the computed C II 1334.532, 1335.663, and 1335.708 Å resonance lines are smaller than observed and display weak central reversals.

We now focus on the upper chromospheric lines. For the very abundant elements the low oscillator strength (i.e., low gf) lines form near the base of the upper chromosphere. Unlike the low-FIP elements continua, the lines never have a low-chromospheric component because of their high temperature sensitivity. This is the case of the C I lines shown in Figure 12. One of these lines (1468.41 Å) and the line and adjacent continua were used for the intensity histogram in Section 2 for all quiet-Sun components. The results shown here for the quiet-Sun components match different ranges of the intensity distribution for both the line and the continuum. Also, the match between the computed and observed line average quiet-Sun profiles is very good for the weak C I 1472.2 Å line (between our levels 1 and 16) which has a small strength gf $\sim$ 0.00078. This line forms mainly at the base of the upper chromosphere and has a maximum intensity contribution function at $p \sim 66$ dyne cm^{-2}. In the case of the stronger, gf $\sim$ 0.0031, C I 1470.1 Å line (between levels 1 and 17) the computed peak intensities are 30% larger than the observed. The maximum of the intensity contribution
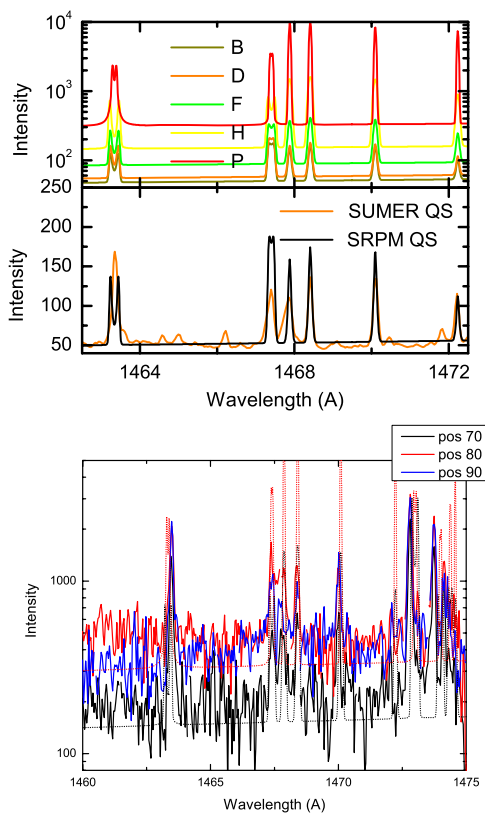
Figure 12. Lines and continuum in the interval 1462–1473 Å computed for all models (top panel), in the average quiet-Sun (middle panel) and in plage (bottom panel). In the bottom panel, SUMER observations are shown in solid line and the results from models 1004 and 1005 are plotted in dot lines.

function occurs slightly higher, at p $\sim$ 56 dyne cm^{-2}. For another case, the C I 1468.4 Å line (between levels 1 and 18, with gf $\sim$ 0.0038 the computed peak intensities are 40% larger than the observed. In the case of the much stronger, gf $\sim$ 0.053, C I line (between levels 1 and 19) the computed peak intensities are 70% larger than the observed. Figure 12 displays a clear pattern where the C I lines at shorter wavelengths have increasing upper level energy and larger gf values. Thus, the collisional excitation rate of the shorter wavelength lines have increasing temperature dependence, and because of the increasing gf these lines also form higher in the atmosphere. The excess of the computed emission seems to indicate some issue in the model above the base of the upper chromosphere, but it does not unambiguously resolve it. Note also that the computed C I 1467.4 Å line profile displays a small central reversal that is not observed. Furthermore, the C I 1463.3 Å line (between levels 1 and 20) has a relatively large strength, gf $\sim$ 0.422, and forms close to the top of the upper chromosphere with the maximum of the intensity contribution function at p $\sim$ 0.63 dyne cm^{-2}. In the calculations, this line has a deep central reversal and the two peak intensities are slightly lower than the single peak displayed in *SOHO*/SUMER data. The collision strengths used for these transitions are fairly reliable and are based on those given by Dunseath et al. (1997). The values were tabulated for somewhat higher temperatures than those in the upper chromosphere, and we extrapolated them to lower temperatures using a log–log interpolation, or in other cases used the Burgess & Thully (1992) method.

The central reversals of strong lines cannot be eliminated by a simple change in the model temperatures. If one were to reduce the temperature in the top layers of the upper chromosphere,

then the stronger lines would develop an even deeper central reversal. Also, these reversals cannot be eliminated by a change in heights, for the given pressures, compatible with the observations at the limb. If the extension of the upper chromosphere is reduced then central reversals will diminish, but in order to reproduce the complete lack of central reversal this extension would be narrower than the limb observations indicate. Note that in any adjustment attempted, the transition-region pressure needs to be maintained for the results to produce transition-region line ratios and Lyα intensity compatible with the observations. A solution for the issue of self-reversals in strong lines is to assume that above the base of the upper chromosphere the material at chromospheric temperatures does not fill all the space in the upper transition-region resolution element. In this way, the optical thickness of the upper chromosphere in the strong lines would not increase as much as it would by the increase of the gf values.

To explore the effects of model changes we compare the lines we compute with those obtained by AL, using a different model and NLTE code. The AL paper shows in Figures 11 and 12 the lines C I 1328.834 Å, 1329.1 Å (which has three components), and 1329.577 Å (with two components) that correspond to transitions between our levels 1 and 14 and have gf values greater than or equal to 0.1 (when the components of each of the blends are added). These figures show line profiles directly resulting from the radiative transfer calculation before applying their convolution. The AL calculations also obtain a central reversal that is not observed. To eliminate this reversal, AL convolves the computed profiles with a very wide and arbitrary bandpass. Such convolution is applied after the NLTE and profile computations are carried out, as is usually done for macro-turbulence. This was done because these authors compare their calculations with the average quiet-Sun spectra and assume smearing due to velocities. However, in *SOHO*/SUMER spatially resolved data, at a resolution of $\sim$2 arcsec, there is never an indication of any self-reversals in lines other than the resonance lines of hydrogen and helium. Moreover, profiles as narrow as the AL computed before convolution are never observed. Consequently, the assumption in AL of macro-turbulence being responsible for the large line broadening and lack of central reversals is inconsistent with the observations.

Our computations use the same non-thermal line broadening for both the NLTE and emitted profile calculations and, unlike the AL, do not apply further convolutions other than with the known *SOHO*/SUMER instrument resolution (FWHM $\sim$ 40 mÅ in the first order). We find that the strong line profiles are about as broad as the observed but still display the unobserved central reversal in the strong lines. (The non-thermal line broadening parameters we use are listed in the electronic tables, which are available in a supplementary tar file in the online edition of the journal, and were shown in Fontenla et al. 2008.) These broadening values are consistent with convective motions in the photosphere and low chromosphere; but increase with the temperature up to about $\sim$12 km s^{-1} in the upper chromospheric plateau. It is verified here that the *SOHO*/SUMER instrument resolution preserves the basic line profiles and does not eliminate the computed central reversal. For the comparison with irradiance observations, however, convolution with the $\sim$1 Å FWHM bandpass of both SORCE/SOLSTICE and EVE was performed. The current irradiance measurements are not capable of resolving the central reversals of lines, not even in the case of the broad Lyα line.

The issue about the unobserved central reversal of strong lines is also evident in other strong lines of various abundant
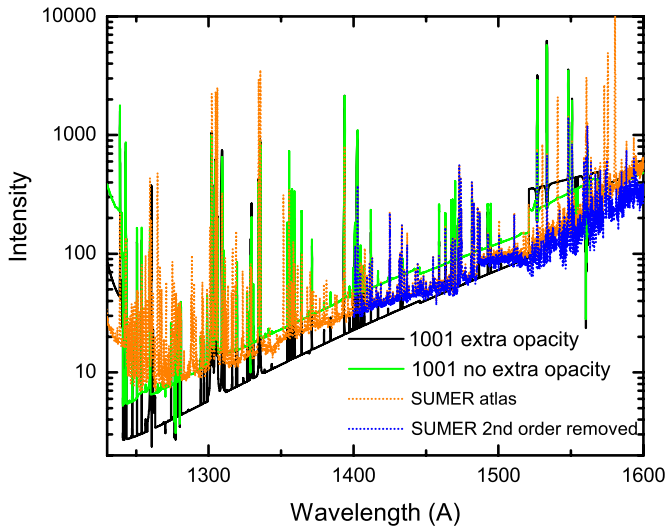
Figure 13. FUV disk-center radiance from model 1001 using SRPM with and without the "extra" continuum included in the NLTE computations, compared with the *SOHO*/SUMER quiet-Sun spectrum. Also shown is part of the *SOHO*/SUMER spectrum after removal of the second-order contamination.

species (e.g., O I and Si II) and in all the model atmospheres we compute. This rules out explanations based on sensitivity to the atmospheric model or the C I collisional excitation rates. The computed strong lines Si II 1304.37 and 1309.276 Å (levels 1–5, gf ∼ 0.18 and 0.34, respectively), and the 1260.422 Å (levels 1–6, gf ∼ 1.91) have deep central reversals that are not observed, but their width is not very different from the observed. (AL also computed these lines, but do not show their unconvolved profiles for these lines. In their plots the convolution erases the computed line profiles and artificially distorts the computed profiles to obtain a relatively good agreement with the observations.)

6. THE FUV CONTINUUM AND THE "MISSING" UV OPACITY

A large effect of the photospheric continuum and absorption lines in the UV on the photoionization of neutral species in the chromospheres of radiative equilibrium stellar models has been published (e.g., Short & Hauschildt 2005; Fuhrmeister et al. 2006). Also, stellar models have problems explaining the observed spectrum and a "missing" UV opacity has often been discussed in the literature (e.g., Short & Lester 1994). However, those models do not reproduce the solar EUV/FUV observed spectrum studied here. The stellar radiative equilibrium models are very different from solar models because they lack the upper chromosphere that is required to match the observed solar FUV and EUV line and continuum emissions.

The present analysis indicates that in the models presented here photospheric irradiation has significant effects only in the near-UV range ∼1650–3600 Å, in which the lower chromospheric continuum opacity is relatively small, and many deep absorption lines are shown in the high-resolution observations. However, at wavelengths shorter than ∼1650 Å, the bound-free transitions from low FIP species such as Si, Mg, and Fe produce very large absorption in the photosphere and low chromosphere and consequently block the photospheric UV radiation.

The detailed calculations of the photoionization/recombination rates carried out by SRPM consider the effects of H lines, the bound-free continua of all elements, and an "extra" continuum opacity and emissivity to mimic unaccounted or "missing" opacities. The assumed "extra" opacity considered

here is identical and in addition to that of the neutral species of low FIP elements; and the "extra" emissivity is assumed in LTE at and below the temperature minimum, and remains to the temperature minimum value above that layer. In order to assess the effects of "extra" opacity we compared our results with those from PANDORA, and also carried out NLTE computations with SRPM but eliminated this "extra" opacity. The comparison with PANDORA was mentioned above. That code considers the "line-haze" as is described by AL. Differences between the NLTE results from these and SRPM calculations were found to be more affected by the collisional rates and the number and grouping of levels assumed than by the extra opacity and line-haze differences.

The SRPM calculations without "extra" opacity were performed for model 1001 (feature B) by leaving the temperatures and heights unchanged, but readjusting the density by the pressure balance equation. The pressure changes in each run correspond to the changes in electron density resulting from the updated NLTE in each case.

From our calculations we find that for layers around the temperature minimum in the present models, the values of the NLTE departure coefficients are much lower than unity for the ground levels; and are closer to unity for higher levels. This indicates that in these regions of our models the main source for the de-population of low-lying levels is the irradiation from the upper chromosphere and not the photospheric irradiation. The downward penetration of the upper-chromosphere radiation into lower-chromospheric layers is controlled by the optical thickness between the base of the upper chromosphere and such layers, and therefore is affected by the assumptions regarding "extra" opacity.

Figure 13 shows the FUV spectrum from the calculations without "extra" opacity and the main SRPM calculation compared with that observed by *SOHO*/SUMER. This figure also shows the part of the *SOHO*/SUMER quiet-Sun spectrum that was corrected for second-order overlap. The computed continuum at wavelengths shorter than ∼1200 Å agrees very well with the observations when including the "extra" opacity. Excluding the extra opacity the computed intensities are too high. The continuum emissivity in this spectral range is produced by recombination of several species including S II and C II and is proportional to the value of ($n_e \, n_{ion}$), where n_e is the electron density and n_{ion} is the density of the recombining ion. Because these are high FIP elements they are mostly neutral throughout the chromosphere and the corresponding opacities are proportional to the hydrogen density, n_H. Therefore, the optical depth is simply proportional to the hydrogen column density. The emissivity is proportional to the density of their singly ionized stages, n_{ion}, which is a strong and complicated function of temperature and density. The increased continuum intensity shortward of ∼1200 Å in the computation without "extra" opacity is produced by an increase of ∼20% in the transition region pressure.

Also, the elimination of the "extra" opacity produced an increase in the continuum intensity in the ∼1300–1500 Å range that is shown in Figure 13. The continuum emissivity in this spectral range is due to recombination of Si II, Mg II, and Fe II (and other low FIP elements). Because in the chromosphere these elements are mainly singly ionized, this emissivity is simply proportional to ($n_e \, n_H$), and the temperature value has very little direct effect. Therefore, the total emission is proportional to the emission measure, i.e., the integral of ($n_e \, n_H$) over the depth of the region where the optical depth is ⩽ 1. The continuum opacity in this wavelength range is

primarily due to photoionization of Si I, Mg I, and Fe I which lead to an optical depth of unity near the top of the low chromosphere, and in the present models optical depth unity occurs just below the temperature minimum for the ~1450 Å radiation.

Considering the 1450 Å wavelength as representative of the issues of the FUV continuum, we find that there are only minor differences on the location of the optical depth unity between all the runs. In all cases, this point is slightly below the layer of minimum temperature, at a pressure of ~104–119 dyne cm^{-2}. The Si I number densities are slightly different in the three runs but only with variations of about 10%. However, the emergent intensities are different because the electron density in the neighborhood of the temperature minimum layer (height ~800 km) is substantially different in the three calculations. Our numerical experiments verify that, as expected from the previous discussion, the emergent intensities in each case are nearly proportional to the electron density in the various cases.

Furthermore, the reason for the change in the electron density at the temperature minimum is photoionization by irradiation from the upper chromosphere. This is related to the radiative losses shown in Figure 14, which shows negative radiative losses just below the upper chromosphere at all wavelengths, and especially important in the 2000–4000 and 1000–2000 Å ranges. This photoionization frees electrons that then recombine with Si II, Mg II, Fe II (and other ions of low FIP elements), thereby emitting photons in the entire FUV spectral range. For this process the details of the UV opacity in the geometrically narrow intervening region between the base of the upper chromosphere and the temperature minimum are critical. The difference between our "extra" opacity and the "line-haze" in PANDORA reflects in a difference in emitted intensity of over a factor of 2 at the 1450 Å wavelength. The elimination of the extra opacity increases the emergent intensity by a factor of nearly 4.

The combination of "missing" EUV/FUV opacity at relatively low temperatures in the interface between lower and upper chromospheres and the dependence of the electron density on the overall model produces some uncertainty. There is no direct observational diagnostic for the details of the temperature increase in the region above the temperature minimum other than the emergent intensity in the FUV continuum we discuss here. From theoretical and observational considerations it is unlikely that a purely plane-parallel structure actually exists; instead a rough and time-dependent interface is expected between the lower and upper chromospheres. As pressure decreases through this interface, the chromospheric electron heating turns from ineffective at the bottom to very effective at the top.

The "extra" opacity in the ~1300–1600 Å range seems to be mainly continuum, because of the lack of absorption lines in the observed spectrum. If lines were responsible for the bulk of this extra opacity then the observed spectrum would exhibit important variations with wavelengths that are not observed at the high spectral resolution of *SOHO*/SUMER. Also, high spatial resolution (~1 arcsec) and medium spectral resolution (0.2 Å) data are available for the Mg II h and k lines (Morrill & Korendyke 2008). After examining these data it is apparent that not only lines, but also missing continuum opacity seems to be present and we are currently considering several sources not yet included, e.g., SiH+, MgH+, FeH+. Also, we are currently performing experiments including NH photodissociation from Kirby & Goldfield (1991) and find that this is an important opacity component.

None of the current approximations for the missing UV opacity and emissivity are rigorously justified. The opacity and source function of molecular continua and lines can generally be computed in LTE, but the atomic continua and lines depart from LTE in the chromosphere. Early attempts to solve these issues were made. Haberreiter et al. (2008) considered NLTE in determining the species ionization, and AL introduced a scattering albedo formulation with height-dependent values for the line source function. However, these approaches are very schematic, do not consider all effects and do not thoroughly consider in detail all the transitions between all the levels and with the continuum. In order to properly compute the near-UV intensities from models we plan to include in future work the effects on the photoionization of lines computed with full NLTE for all relevant species. From our sensitivity studies we find that the most significant effects of photospheric irradiation occur in the near-UV 2000–3600 Å spectral range due to many absorption lines of species not considered here, such as Ni, Cr, V, Ti, Mn, and Fe III. In addition, irradiation by emission lines in the upper chromosphere and transition region is expected to be significant at wavelengths shorter than ~1600 Å.

7. RADIATIVE LOSSES

The radiative losses are often computed for each species. However, here we compute them by wavelength interval by including all atomic/ionic species/molecules. Figure 14 shows the results for a few wavelength intervals in which these radiative losses are of great importance for the upper chromospheric and low transition-region energy balance.

In the present paper, radiative losses from several less abundant species have not been computed (e.g., Ni, Cr, Ti, V, Mn, in their first three ionization stages, and also Fe III). These species have significant lines in the 2500–4000 Å range, but are probably not very important for the upper chromosphere and lower transition region.

Figure 14 shows the computed radiative losses per unit volume for the quiet- and active-Sun components (sunspots are excluded) as a function of height for several wavelength intervals. Part of this energy escapes into space, but another part is emitted downward and absorbed in the lower chromosphere producing radiative heating in these layers. Negative radiative losses (i.e., radiative heating) are shown by dotted lines. The figure illustrates heating of the upper chromosphere by radiation in the 300–1000 Å range, however, this heating is small and is compensated by losses at other wavelengths. Radiative heating in the lower chromosphere occurs at most wavelengths in the figure, and for all models, but it is weak and compensated by losses at longer wavelengths not shown.

A very important cooling source near the temperature minimum is CO infrared bands. Fontenla et al. (2008) showed that radiative balance is achieved in the lower chromosphere of the inter-network within the margin of error of the present model 1001. We have not yet computed the radiative losses at all wavelengths for the other models. From partial calculations, we find that some small positive value of the total radiative losses occur in the plage and facula models that could be balanced by relatively weak magnetic heating (due to Joule effect; see Farzad & Goodman 2006).

Variations in the distribution of the radiative losses with pressure (or height) are present in these graphs and they generally correspond to spectral lines that radiate strongly at some wavelengths and in certain layers. Particularly noticeable in the 300–1000 Å interval are the transition-region lines that
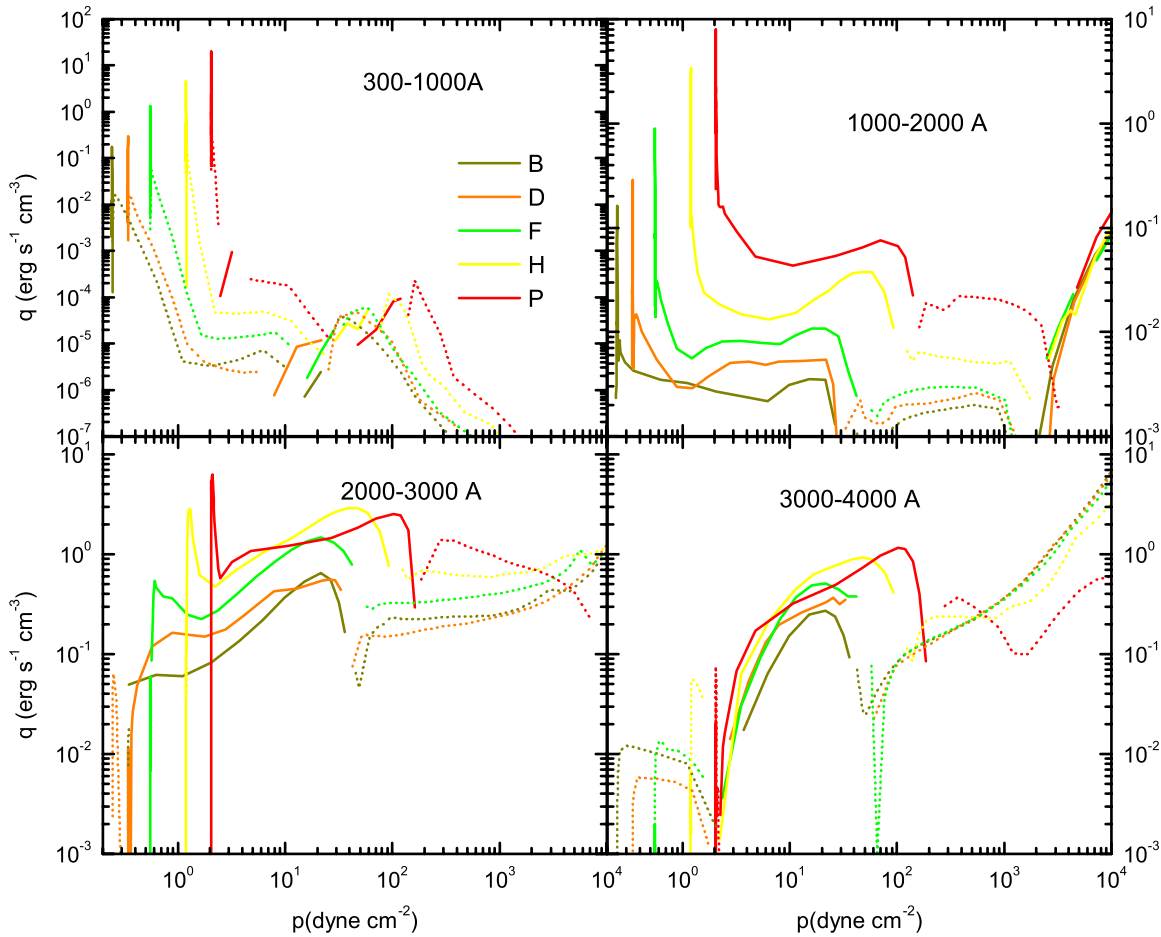
Figure 14. Radiative losses per unit volume in erg s^{-1} cm^{-3} as a function of pressure for each of the models and in several spectral bands. The dotted lines correspond to negative values (i.e., radiative heating). The identification colors shown in the first panel for the curves apply to all panels.

produce the sharp increase at the nearly constant pressure of the transition region in each model. Similarly, the Lyα peak in the lower transition region is displayed in the 1000–2000 Å interval. The Mg II line centers, in the 2000–3000 Å interval, produce a peak at the base of the transition region and their wings are important throughout the entire upper chromosphere. In the 3000–4000 Å interval, the Ca II lines are very important contributors throughout the upper chromosphere. However, apart from the contributors just mentioned, a large number of emission lines are also important even when they do not display identifiable peaks in these graphs.

Figure 15 shows the radiative losses function versus temperature. This function corresponds to the radiative losses scaled by the product of the electron and total hydrogen densities (e.g., see FAL 2). This figure shows that throughout the transition region the radiative losses are not far from a simple relationship with densities. However, there are still important radiative transfer effects that determine the shape of this relationship and produce somewhat different curves for different models. The current models have similar shapes of temperature versus pressure profile, but if these shapes were different then that would affect the shape of the radiative losses function shown in this figure.

An important issue is the increase in the radiative losses with increasing magnetic activity. Table 3 shows, for several spectral bands and for each model, the radiative losses per unit volume integrated over all heights within the upper chromosphere and the low transition region. The integral over height corre-

Table 3
Total Radiative Losses in erg s^{-1} cm^{-3} from the Upper Chromosphere and Low Transition-region in Several Wavelength Ranges, for Five of the Models

Model	300–1000 Å	1000–2000 Å	2000–3000 Å	3000–4000 Å
1001 (B)	1.14e5	5.18e5	1.99e7	6.32e6
1002 (D)	0.99e5	6.99e5	2.00e7	1.01e7
1003 (F)	2.11e5	1.23e6	6.35e7	1.58e7
1004 (H)	4.04e5	3.00e6	1.44e8	3.77e7
1005 (P)	7.77e5	7.69e6	1.46e8	4.56e7

sponds to the layers located above the temperature minimum and where the temperature values are $T > 5000$ K. The table shows that the total radiative energy losses for the entire spectral range 300–4000 Å are comparable or less than the available energy at the temperature minimum for dissipation by the Farley–Buneman instability, as is estimated by Table 1 in Fontenla et al. (2008). Therefore, we find that our radiative loss estimates are consistent with the scenario for chromospheric heating proposed in that paper.

Note that the radiative losses in Table 3 for the inter-network model upper chromospheric layers are a factor between 2 or 3 larger than those by Anderson & Athay (1989) showed for the quiet-Sun (see their Figure 7). The current calculations include more species and transitions than those Anderson and Athay considered; moreover, because our model 1001 is different from any they considered, the shape of the radiative loss we obtain differs significantly from the radiative loss function in their Figure 9.
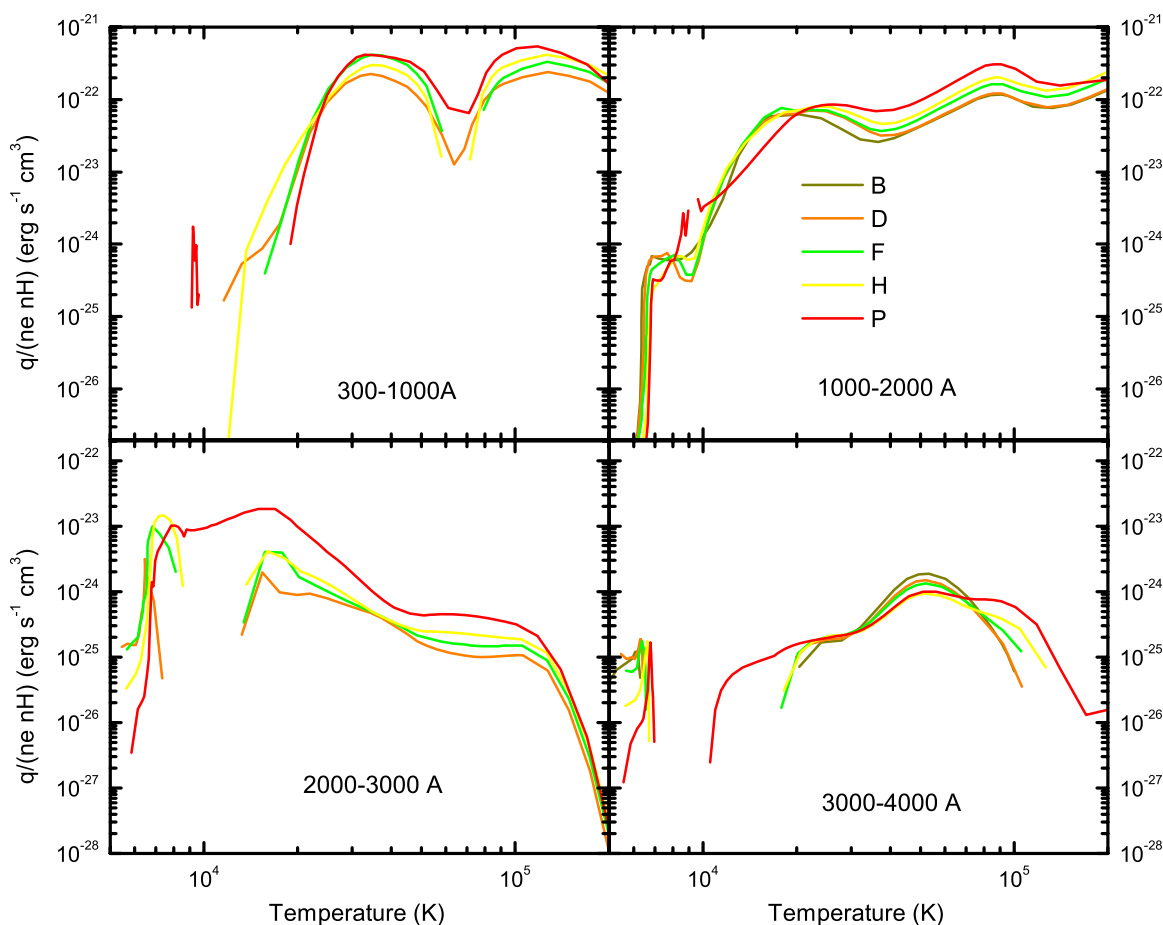
Figure 15. Scaled radiative losses, or radiative loss functions, as functions of temperature for the models of atmospheric features. The units are erg s^{-1} cm^3 and correspond to the radiative losses per unit volume divided by the product of electron and total hydrogen densities.

In Table 3, the radiative losses at wavelengths longer than 2000 Å are larger than those at shorter wavelengths and this is due mostly to the Mg II and the Ca II line cores and wings, but other species also contribute. These losses have a broad relative maximum at the base of the upper chromosphere, as shown in Figure 14, except for the sharp features at lower pressures. The data in Table 3 along with Figure 14 show that, when integrating over height, the total upper chromospheric radiative losses are considerably larger than those in the lower-transition region. The radiative losses at wavelengths shorter than 2000 Å are more distributed over the upper chromosphere and have very large peaks at the lower transition region. We refer to the FAL 1–4 papers for the explanation of the peaks due to the contribution of H (particularly Lyα) and He lines to those peaks. Here we just mention that most of the transition region energy can be explained by energy down flow from the corona. Mechanical dissipation, at a level comparable to that in the chromosphere, does not contribute much to balance the radiative losses of the low transition region.

8. DISCUSSION AND CONCLUSIONS

In this paper, we derived a set of models that matches line profiles and contrasts of the visible observed spectrum and are consistent with recent observations of spectral irradiance variations. These data are useful for the synthesis of the solar irradiance spectrum using the methods described in Fontenla et al. (1999) and Fontenla & Harder (2005).

However, the most important issues discussed in this paper concern the EUV/FUV continuum and lines that are produced in the chromospheric layers of these models. The models presented in this paper reproduce the observed EUV continuum, and approximately reproduce the observed FUV continuum and upper chromospheric weak lines.

We show how monochromatic intensity histograms can be used to characterize spatially resolved spectra of the quiet-Sun and define a set of solar features. The quiet- and active-Sun features are defined by their intensity thresholds at certain wavelengths and the entire solar irradiance spectrum can be obtained from the distribution of these features over the solar disk. Tables of the physical parameters that describe the structure of the various models are available on the Web site http://www.digidyna.com and are also available by email request to fontenla@colorado.edu. The SRPM computing system produces a very detailed complete spectrum for each of these models, at various observation angles. Portions of these data are also available when requested via email to the previously mentioned address.

The radiative losses as functions of height were computed for all models for several wavelength ranges. The values obtained for the quiet-Sun inter-network are compatible with those by Anderson & Athay (1989), and the values for network and active regions are substantially larger than those for the inter-network, as is expected. The upper chromospheric radiative losses for the five models studied in detail here are broadly consistent with those proposed by Fontenla et al. (2008) to correspond to the Farley–Buneman instability.

Important issues are the UV opacity and emissivity not accounted for by well known processes, and the effects of

lines in the photoionization. In the near-UV, a large number of absorption lines affect the emitted intensities. Their effect on the photoionization transition rates can have some consequences on low-FIP elemental ionization in the low chromosphere. This is especially valid in radiative-equilibrium stellar models because in these cases there is no solar-like upper chromosphere, and the UV irradiation of the chromosphere essentially originates in the photosphere. To establish the importance of the near-UV lines in solar models, very detailed full-NLTE computations are needed that must consider relatively low abundance elements whose atomic properties are presently not too well known.

However, in the solar chromosphere, the FUV and EUV observed emissions in continuum and lines produced in the upper chromosphere and transition region irradiate the low chromosphere and have significant effects on the ionization. In the present modeling, we introduce an ad hoc "extra" opacity and emissivity that reduces the irradiation of the temperature minimum region by the upper chromosphere. The origin of this "extra" opacity is not well understood, and may be related to the so-called missing UV opacity in stellar astrophysics. In our opinion, the "extra" opacity and emissivity are basically of continuum nature because no significant absorption lines and only emission lines are observed in the EUV/FUV spectrum at wavelengths shorter than ~1600 Å. (Note that even when atomic lines exist in theory, absorption lines are never observed even at the highest spectral resolution and therefore cannot significantly affect the elemental ionization or level populations computed here.)

The recombination continua of low-FIP elements (e.g., Si ii, Mg ii, and Fe ii) are basically proportional to the chromospheric "emission measure." This quantity is defined as the integral over geometrical depth of the hydrogen density times the electron density up to the point where the optical depth is not too large. This recombination has very weak dependence on the temperature, but the end point of the integration is dependent on the temperature. A large increase in the emitted FUV intensity occurs when the "extra" opacity is removed. This increase is *not* caused by optical thickness changes because the continuum optical depths do not change much, since Si i density in the low chromosphere does not change much when the extra opacity is removed. Instead, the intensity increase is caused by the increased emissivity (photons due to Si ii recombination with electrons) due to the higher electron density values resulting from hydrogen overionization around the temperature minimum layers when the extra opacity is removed. The details of the intervening EUV/FUV opacity between the base of the upper chromosphere and the temperature minimum region are crucial to the hydrogen overionization around the temperature minimum and thereby affect the electron density in these low temperature layers. Through the electron density these processes determine the low-FIP elements continuum emissivity and thereby the emitted FUV continuum.

The transition-region layers included in this paper, with temperatures below 2×10^5 K, are still preliminary because fully consistent energy balance calculations have not yet been carried out. The present results for the radiative losses and line ratios will permit us to resolve these issues by improving the current transition-region models to make them fully consistent and to reconcile them with the EUV and FUV observations. The transition region and coronal lines illuminate the upper chromosphere and affect the elemental ionization and some levels population (e.g., the He i; see Avrett et al. 1994 and Centeno et al. 2008), but this effect has not yet been considered.

Measured values of the outgoing flux are available, but are affected by transition region and chromospheric emissions already included in our calculation. Therefore, introducing an irradiation using the observed emitted intensity values would unjustifiably double some contributions that are already accounted for.

Our computations reproduce well the observed detailed profiles of the low "gf" lines from the base of the upper chromosphere. For this, we consider a microturbulent non-thermal line broadening that suddenly increases as the non-radiative heating develops in the upper chromosphere. This line broadening is small at the low chromosphere and is compatible with the granular motions there. In all cases, the non-thermal line broadening is used consistently in the full NLTE calculations and in the computation of the emitted intensity. The only convolution we perform is with the instrument resolution of the data with which we compare our computed spectrum.

The computed detailed profiles of the strong resonance lines formed near the top of the upper chromosphere and the base of the transition region generally display a self-reversal that is incompatible with the *SOHO*/SUMER observations. The line emissivity is sensitive to the "emission measure," but in contrast to the continuum it is very sensitive to the temperature as well. The strong lines central reversal can disappear if the temperature increases with height rapidly enough, but this is not feasible given the constraints of matching the whole spectrum. Another possibility of solving the issue of central reversals is to consider particle diffusion within the regions where strong ionization gradients occur in all species. As mentioned earlier, we consider particle diffusion for hydrogen but not yet for other species. As FAL 3 and 4 showed, diffusion and velocities have important effects in He as well, and as preliminary calculations by Fontenla (2005) showed, diffusion is likely to also affect other species such as C and O.

As a possible solution to reconcile the observed intensity of the strong lines with the modeling, we propose to consider that the top of the upper chromosphere is not a dense layer, but instead it is formed by a collection of loops at various temperatures and reaching various altitudes. In this scenario, as loops of lower apex close, the loops are packed closely at lower heights but more sparsely at larger heights. This matches high-spatial-resolution imaging observations that show structures of this type. Comprehensive study of this structure requires a full three-dimensional analysis and is beyond the scope of the present paper.

Flows are expected to occur in a picture of intermittent heating of chromospheric loops, with near granular scales in the quiet-Sun, with larger scales in the magnetic network, and with even larger scales in active regions. Strong flows could also affect the relatively slow elemental ionization/recombination, but it is not possible to assess in which way because the nature of the intermittency and flows is critical and not yet fully characterized. It is important to perform full simulations of three-dimensional chromospheric fine structure considering very detailed full-NLTE radiative transfer calculations. Such calculations must be able to fully describe not only the MHD properties, but also the detailed radiative interactions between all plasma components. Also, the simulation must address the proposed chromospheric heating mechanisms. When considering the Farley–Buneman instability, it needs to at least be multi-fluid, considering not only protons and electrons but also neutral hydrogen and the heavy ions that dominate the plasma quasi-neutrality in the low chromosphere.

From the spectral irradiance point of view the details of the three-dimensional "microscale" features that compose the chromosphere are not as important as the averaged properties. However, those details and the "microscale" structure are very important for (1) understanding intrinsic physical processes, (2) being able to obtain models more consistent with the basic physics, (3) eliminating arbitrary and ad hoc parameters and values, and (4) understanding how the various layers and phenomena interact. Finally, the dependence of the overall chromosphere on the magnetic fields can only be investigated by using empirical correlations, but it cannot be completely and unambiguously established until the "microscale" processes are well understood.

Even at medium resolution, a strictly one-dimensional approach is a very crude physical description for the strongly inhomogeneous upper-transition-region and coronal layers. However, the detailed geometrical parameters of the inhomogeneities are not critical for the optically thin emitted flux but only the mix of emitting volumes is important. Therefore, a pseudo-one-dimensional approach is adequate for evaluating the irradiance due to quiet-Sun and active region bulk emission from the composite upper chromosphere, transition-region, and corona. In such an approach, a filling factor for each type of feature is used at each solar radius. The juxtaposition of the different solar features needs to be considered when examining center-to-limb behavior of the radiance because several features will be present along any line of sight. In spite of their simplicity, such models might help us estimate the EUV solar irradiance at Earth and the radiation incident on the chromosphere.

In yet unpublished work, we have applied the computed visible and infrared spectra produced by the models herein to the synthesis of the solar irradiance spectrum. Similar work for the FUV and EUV spectrum is underway. These methods so far assume that solar spectral irradiance variations are exclusively due to solar activity, or network features observable in contrast images. However, changes of the areas not identified as magnetically "active" in the images used are possible, and according to SORCE/SIM observations over the decay of the last solar cycle (Harder et al. 2009) these changes are likely. The current methods permit us to isolate the observed features from behavior due to other processes and thereby address the issue of changes in the "quiet-Sun." Separate papers will address the comparison between these results and the observations by the SORCE/SIM instrument during the solar activity cycle 23.

REFERENCES

Anderson, L. S., & Athay, G. 1989, ApJ, 346, 1010

Aschwanden, M. J., Nightingale, R. W., Tarbell, T. D., & Wolfson, C. J. 2000, ApJ, 535, 1027

Avrett, E. H. 2009, in Numerical Methods for Multilevel Radiative Transfer Problems, ed. R. Rannancher & R. Wehrse (Heidelberg: Springer)

Avrett, E. H., Fontenla, J. M., & Loeser, R. 1994, in IAU Symp. 154, Infrared Sol. Physics, ed. D. M. Rabin, J. T. Jefferies, & C. Lindsey (Dordrecht: Kluwer), 35

Avrett, E. H., & Loeser, R. 2003, in I.A.U. Symp. No. 210, Modeling of Stellar Atmospheres, ed. W. Weiss & N. Piskunov (Dordrecht: Kluwer), 14

Avrett, E. H., & Loeser, R. 2008, ApJS, 175, 229 (AL)

Ayres, T. R., & Rabin, D. 1996, ApJ, 460, 1042

Bautista, M. A. 1997, A&A, 122, 167

Buneman, O. 1963, Phys. Rev. Lett., 10, 285

Burgess, A., & Thully, J. A. 1992, A&A, 254, 436

Centeno, R., Trujillo Bueno, J., Uitenbroeck, H., & Collados, M. 2008, ApJ, 677, 742

Chamberlin, P. C., Woods, T. N., Crotser, D. A., Eparvier, F. G., Hock, R. A., & Woodraska, D. N. 2008, Geophys. Res. Lett., 36, L05102

Cincunegui, C., & Mauas, P. J. D. 2001, ApJ, 552, 877

Cox, D. P., & Tucker, W. H. 1969, ApJ, 157, 1157

Curdt, W., Brekke, P., Feldman, U., Wilhelm, K., Dwivedi, B. N., Schühle, U., & Lemaire, P. 2001, A&A, 375, 591

Curdt, W., Tian, H., Teriaca, L., Schühle, U., & Lemaire, P. 2008, A&A, 492, L9

Delbouille, L., Roland, G., Brault, J., & Testerman, L. 1981, Photometric Atlas of the Solar Spectrum from 1850 to 10,000 cm^{-1} (Tucson, AZ: Kitt Peak Natl. Obs.)

Dere, K. P., Landi, E., Mason, H. E., Monsignori Fossi, B., & Young, P. R. 1997, A&AS, 125, 149

Doschek, G. A., Feldman, U., Laming, J. M., Warren, H. P., Schühle, U., & Wilhelm, K. 1998, ApJ, 507, 991

Doschek, G. A., & Mariska, J. T. 2001, ApJ, 560, 420

Dufton, P. L., & Kingston, A. E. 1994, At. Data Nucl. Data Tables, 57, 273

Dunseath, K. M., Fon, W. C., Burke, V. M., Reid, R. H. G., & Noble, C. J. 1997, J. Phys. B: At. Mol. Opt. Phys., 30, 277

Ermolli, I., Criscuoli, S., Centrone, M., Giorgi, F., & Penza, V. 2007, A&A, 465, 305

Farley, D. T., Jr. 1963, J. Geophys. Res., 68, 6083

Farzad, K., & Goodman, M. L. 2006, ApJS, 166, 613

Fontenla, S. 2005, BAAS, 38, 237

Fontenla, J. M., Avrett, E. H., & Loeser, R. 1990, ApJ, 355, 700 (FAL 1)

Fontenla, J. M., Avrett, E. H., & Loeser, R. 1991, ApJ, 377, 712 (FAL 2)

Fontenla, J. M., Avrett, E. H., & Loeser, R. 1993, ApJ, 406, 319 (FAL 3)

Fontenla, J. M., Avrett, E. H., & Loeser, R. 2002, ApJ, 572, 636 (FAL 4)

Fontenla, J. M., Avrett, E., Thuillier, G., & Harder, J. 2006, ApJ, 639, 441 (Paper I)

Fontenla, J. M., Balasubramaniam, K. S., & Harder, J. 2007a, ApJ, 667, 1243 (Paper II)

Fontenla, J. M., Curdt, W., Avrett, E. H., & Harder, J. 2007b, A&A, 468, 695

Fontenla, J., & Harder, J. 2005, Mem. Soc. Astron. Italiana, 76, 826

Fontenla, J. M., Peterson, W. K., & Harder, J. 2008, A&A, 480, 846

Fontenla, J., Reichmann, E. J., & Tandberg-Hanssen, E. 1988, ApJ, 329, 464

Fontenla, J. M., & Rovira, M. 1985a, J. Quant. Spectrosc. Radiat. Transfer, 34, 389

Fontenla, J. M., & Rovira, M. 1985b, Sol. Phys., 96, 53

Fontenla, J. M., White, O. R., Fox, P. A., Avrett, E. H., & Kurucz, R. L. 1999, ApJ, 518, 480

Fuhrmeister, B., Short, C. I., & Hauschildt, P. H. 2006, A&A, 452, 1083

Goldman, A., Schoenfeld, W. G., Goorvitch, D., Chackerian, C., Dothe, H., Jr., Mélen, F., Abrams, M. C., & Selby, J. E. A. 1998, J. Quant. Spectrosc. Radiat. Transfer, 59, 453

Griffiths, N. W., Fisher, G. H., Woods, D. T., & Siegmund, O. H. W. 1998, ApJ, 512, 992

Haberreiter, M., Schmutz, W., & Hubeny, I. 2008, A&A, 492, 833

Harder, J., Fontenla, J., White, O., Rottman, G., & Woods, T. 2005, Mem. Soc. Astron. Italiana, 76, 735

Harder, J. W., Fontenla, J. M., Pilewskie, P., Richard, E. C., & Woods, T. N. 2009, Geophys. Res. Lett., 36, L07801

Harvey, K. L., & White, O. R. 1999, ApJ, 515, 812

Holweger, H., & Müller, E. A. 1974, Sol. Phys., 39, 19

Kirby, K. P., & Goldfield, E. M. 1991, J. Chem. Phys., 94, 1271

Kopp, G., Lawrence, G., & Rottman, G. 2005, Sol. Phys., 230, 129

Landi, E., Del Zanna, G., Young, P. R., Dere, K. P., Mason, H. E., & Landini, M. 2006, ApJS, 162, 261

Landi, E., Dere, K. P., Young, P. R., Landini, M., Mason, H. E., & Del Zanna, G. 2005, in ASP Conf. Ser. 13, Highlights of Astronomy ed. O. Engvold (San Francisco, CA: ASP)

Lemaire, P., Emerich, C., Vial, J.-C., Curdt, W., Schühle, U., & Wilhelm, K. 2005, Adv. Space Res., 35, 384

Liu, S. Y., & Sheeley, N. R., Jr. 1971, Sol. Phys., 20, 282

Maltby, P., Avrett, E. H., Carlsson, M., Kjeldseth-Moe, O., Kurucz, R. L., & Loeser, R. 1986, ApJ, 306, 284

Mihajlov, A. A., Ignjatovic, Lj. M., Sakan, N. M., & Dimitrijevic, M. S. 2007, A&A, 469, 749

Mihalas, D., Heasley, J. N., & Auer, L. H. 1975, STIN, 7630128

Monsignori Fossi, B. C., & Landini, M. 1992, Mem. Soc. Astron. Italiana, 63, 767

Morrill, J. S., & Korendyke, C. M. 2008, ApJ, 687, 646

Nahar, S. N., Bautista, M. A., & Pradhan, A. K. 1997, ApJ, 479, 497

Nahar, S. N., & Pradhan, A. K. 1994, J. Phys. B: At. Mol. Opt. Phys., 27, 429

Orozco Suárez, D., et al. 2007, ApJL, 670, L71

Porter, J. G., Fontenla, J. M., & Simnett, G. M. 1995, ApJ, 438, 472

Preminger, D. G., Walton, S. R., & Chapman, G. A. 2001, Sol. Phys., 202, 53

Ralchenko, Yu., Kramida, A. E., Reader, J., & NIST, ASD Team 2008, NIST Atomic Spectra Database (version 3.1.5) (Gaithersburg, MD: NIST) Available online at http://physics.nist.gov/asd3 (2009, February 18)

Rottman, G., Harder, J., Fontenla, J., Woods, T., White, O. R., & Lawrence, G. M. 2005, Sol. Phys., 230, 205

Schühle, U., Wilhelm, K., Hollandt, J., Lemaire, P., & Pauluhn, A. 2000, A&A, 354, L71

Seaton, M. J. 1962, Proc. Phys. Soc., 79, 1105

Short, C. I., & Hauschildt, P. H. 2005, ApJ, 618, 926

Short, C. I., & Lester, J. B. 1994, ApJ, 436, L161

Solanki, S. K., Livingston, W., Muglach, K., & Wallace, L. 1996, A&A, 316, 303

Stancil, P. C. 1994, ApJ, 430, 360

Subramanian, S., Madjarska, M. S., Maclean, R. C., Doyle, J. G., & Bewsher, D. 2008, A&A, 488, 323

Thuillier, G., Herse, M., Labs, D., Foujols, T., Peetermans, W., Gillotay, D., Simon, P. C., & Mandel, H. 2003, Sol. Phys., 214, 22

Tian, H., Curdt, W., Marsch, E., & Schühle, U. 2009, A&A, 504, 239

Tripathi, D., Mason, H. E., Young, P. R., & Del Zanna, G. 2008, A&A, 481, L53

Vernazza, J. E., Avrett, E. H., & Loeser, R. 1981, ApJS, 45, 635 (VAL)

Wallace, L., Hinkle, K., & Livingston, W. 1998, NSO Technical Report No. 98-001, National Solar Observatory (Tucson, AZ: National Optical Astronomy Observatories)

Warren, H. P., & Mariska, J. T. 1998, ApJS, 119, 105

Warren, H. P., Winebarger, A. R., Mariska, J. T., Doschek, G. A., & Hara, H. 2008, ApJ, 677, 1395

White, O. R., Altrock, R. C., Brault, J. W., & Slaughter, C. D. 1972, Sol. Phys., 23, 18

Woods, T. N., et al. 2009, Geophys. Res. Lett., 36, L01101